Overview of recent progress in 3D field physics in KSTAR

Gunyoung Park, Won-Ha Ko, Jaehyun Lee, Minwoo Kim, Giwook Shin, Sang-Hee Hahn, Tongnyeol Rhee, Minjun J. Choi, Kimin Kim, HyungHo Lee, Young-Mu Jeon, Woong-Chae Kim and Siwoo Yoon

Korea Institute of Fusion Energy, Daejeon 34133, Korea

Yongkyoon In

Ulsan National Institute of Science and Technology, Ulsan 44919, Korea

Jong-Kyu Park, SangKyeun Kim, SeongMoo Yang and Qiming Hu

Princeton Plasma Physics Laboratory, Princeton, USA

Various 3D field physics challenges of magnetically confined plasmas arise, when the driving source comes from either an externally applied non-axisymmetric 3D magnetic perturbations or plasma instabilities inside the plasma. Recently, several key outstanding topics of 3D field physics have been extensively studied in the Korean Superconducting Tokamak Advanced Research (KSTAR), such as edge-localized-mode (ELM) control by resonant magnetic perturbation (RMP), error field (EF) control, 3D field effects on rotation & transport, and RMP-induced alteration of divertor heat flux & detachment. KSTAR has a few physically unique features (i.e., high rotation and long pulse plasmas with a low intrinsic EF) and machine/diagnostic capabilities (i.e., 3-row in-vessel control coil and state-of-the-art 2D/3D imaging diagnostics), which have been taken advantage of until now to address critical 3D field physics issues relevant to ITER and K-DEMO. Among many remarkable achievements are there a robust control of n=1 RMP ELM suppression along with a development of its physics basis tools, parameter expansion, optimization, and long-pulse control techniques. Nonetheless, a series of unresolved 3D physics themes as well as limited coverage of 3D field operating regimes have also been identified as future works for the 3D field research in KSTAR. In this paper, we provide an overview about recent progress of KSTAR 3D field physics, and present future plans of KSTAR 3D research toward future fusion reactor.

Keywords: KSTAR, Plasma, Fusion, 3D field physics, Edge-Localized-Modes (ELMs), Resonant Magnetic Perturbation (RMP)

Email: gypark@kfe.re.kr

Fax: +82-42-879-6713

1. Introduction

Thanks to the remarkable progress in fusion research for nearly a half-century, it is foreseen that actual fusion burning plasmas will be realized first in a tokamak, as represented by the International Tokamak Experimental Reactor (ITER) [1] under construction in France and the Korea Demonstration Reactor (K-DEMO) [2]. Although a tokamak itself is an intrinsically axisymmetric device with toroidally symmetric magnetic field $\boldsymbol{B}_0$, such an ideal axisymmetry can never be made perfect due to the various sources of fundamentally non-axisymmetric field (often called intrinsic 'error field (EF)') or externally controlled non-axisymmetric field (often called 'magnetic perturbation (MP)'). For example, an intrinsic EF can be naturally introduced by small imperfections of surrounding magnets and/or slight misalignment of conducting structures. In terms of fusion plasmas, these small departures from ideal axisymmetric configuration in tokamaks tend to cause originally nested magnetic flux surfaces to be broken apart and then possess magnetic island chains, and even to drive up stochastic plasma volume through overlap of the neighboring island chains [3,4]. Experimentally, it has been consistently observed that small non-axisymmetric 3D magnetic fields $\delta\boldsymbol{B}$ of $\delta B/B_0 \sim 10^{-4}$ can greatly degrade stability and confinement of the plasma [5,6], thus need to be properly corrected to prevent any deleterious consequences of non-axisymmetric field such as a major confinement loss or a disruptive MHD instability [7]. On the other hand, several beneficial effects of the 3D magnetic fields have also been discovered, including the effectiveness in suppressing edge-localized-modes (ELMs) in high performance plasmas via resonant magnetic perturbation (RMP) [8,9]. Considering the outbursting ELMs are not only releasing the particle and heat fluxes on the plasma facing components (PFC), but also degrading the core-plasma confinement, the discovery of RMP ELM suppression in DIII-D [10] was subsequently explored and proven effective on multiple devices [11-13]. Specifically, ELMs are presently understood as magnetohydrodynamics (MHD) peeling-ballooning instabilities [14,15] at the tokamak edge and its crash event, which is triggered when the edge pressure gradient or current density becomes sufficiently high, can cause irreparable damage to both divertor and PFC in an ITER-like fusion reactor [16]. Therefore, the overall 3D magnetic fields need to be optimally configured (i.e., in terms of applied 3D spectrum and toroidal mode number) to maximize the benefits of 3D fields in tokamaks, while eliminating any harmful effects of 3D EF. As one might have imagined, complete realization of this task requires sophisticated 3D optimization process [17], in addition to an arduous verification and validation in theory, and an ample exploration in experiments.

Meanwhile, the application of 3D field are often accompanied by significant outward particle and heat fluxes, as clearly observed, for example, in the region of magnetic islands or stochastic region where particle and heat can flow rapidly along the magnetic field lines by parallel collisional transport, or even chaotically in a braided magnetic field [18], leading to a net radial flux with respect to the original magnetic flux surfaces. This needs to be more comprehensibly understood and evaluated quantitatively, because essentially the very same confinement loss mechanism can significantly degrade fusion efficiency [19] in future reactor like ITER and K-DEMO. On the other hand, the 3D-induced turbulence and transport can have a positive effect on the overall plasma operation, as well, in that such an enhanced transport would drive out an undesirable build-up of high-Z impurities [20]. Thus, there must be an optimum level of 3D field strength and topology that is causing an acceptable main ion transport with a high fusion efficiency, while providing enough impurity transport required for an ash removal and impurity exhaust. Divertor target heat flux and its 'wetted' area and detachment are another important theme that can be significantly modified by applied 3D fields [21]. In particular, divertor heat flux peaks should be controlled within a tolerable engineering limit of heat loads on their impinging divertor plates in tokamaks.

It is to be noted that the Korean Superconducting Tokamak Advanced Research (KSTAR) [22] is a medium size superconducting tokamak and has been operating successfully since its first plasma generation in 2008 [23]. As emphasized in Refs. [24,25], KSTAR has several unique features, such as a low intrinsic error field, long pulse operation capability, ITER-like three-row in-vessel control coils (IVCC), and 2D/3D advanced imaging diagnostics. In particular, IVCC is our main resource for generating 3D fields (Fig. 1) and its versatile structure makes it possible to apply various 3D configurations with n=1 and/or n=2 fields. Given the importance of 3-D physics study, it is useful to summarize the relevant aspects as follows: 1) With an extremely low intrinsic EF, the KSTAR plasmas are less vulnerable to disruptive core mode-locking events. Thus, we have been able not only to achieve low-n (particularly n=1) RMP ELM suppression more easily [11,26] but also to clarify various plasma responses against externally applied 3D field unambiguously [27]; 2) With its intrinsic long pulse capability, KSTAR provides a rare opportunity to test real-time 3D field control to maintain both RMP ELM suppression and high plasma confinement simultaneously in a series of long-pulse discharges [28,29]; 3) 3D field physics study based on three rows of in-vessel control coils in KSTAR with various applicable coil phsings (Fig. 1(b)), instead of two rows in other tokamaks, has been not only contributing to resolving various urgent issues of the ITER RMP coils [30] but also to demonstrating more useful 3D optimization with additional degrees of freedom in the 3D coil's phase space [17,31]; 4) 2D/3D advanced imaging diagnostics are capable of giving a detailed spatial structure and temporal dynamics of the T_e turbulence/MHD modes across islands or stochastic regions [32], which are readily useful to benchmark gyrokinetic codes to clarify fundamental transport physics under 3D fields [33]. Thus, various aforementioned 3D field physics studies in KSTAR represent a diverse spectrum of the KSTAR 3D research. Nonetheless, we are also mindful that 3D field operating regimes of KSTAR have usually been limited to high rotation ($V_{tor,ped} > 40km/s$), intermediate & high collisionality ($\nu^*_{e,ped} > 0.2$), and low & intermediate beta ($\beta_N \lesssim 2$) plasmas so far [34]. Here, $V_{tor,ped}$, $\nu^*_{e,ped}$, and β_N denote the toroidal rotation velocity of plasma evaluated at a pedestal top, normalized electron collisionality [35] at the pedestal top, and a normalized ratio of thermal to magnetic pressure [36], respectively. This could be one of the limitations for us to project the 3D field impacts on the future fusion reactors like ITER and K-DEMO, where the prevailing plasmas will be characterized by somewhat different conditions, i.e., low rotation ($V_{tor,ped} \sim 0$), low collisionality ($\nu^*_{e,ped} \sim 0.1$), and high beta plasmas ($\beta_N \sim 3.5$ for K-DEMO). Therefore, future 3D field physics study in KSTAR, as will be described in detail in section 6, needs to focus on these more ITER- and DEMO-like plasma regimes to resolve any remaining uncertainties associated with 3D field physics.

In this paper, we provide an overview of the recent progress in 3D field physics research in KSTAR, including various experimental and simulation results, along with a brief discussion of future research directions in 3D field physics. Section 2 provides research highlights of recent RMP ELM control studies in KSTAR. Section 3 discusses intrinsic EF measurements and a novel EF correction scheme. Section 4 presents various experimental and analysis results related to the 3D field effects on rotation & transport studied in KSTAR. Section 5 describes 3D field effects on divertor target heat flux in comparison with the cases without 3D fields. Section 6 provides brief outline of future research plan of 3D field physics toward ITER and K-DEMO. The final section is concluded with a summary of results.

2. Edge-localized-mode (ELM) control by RMP

Despite significant progress on RMP ELM control during the last decade, the physics of the ELM suppression is far from perfect yet, although RMP field penetration and associated stochastic layer formation in the plasma edge have been broadly identified as key physics processes governing RMP-induced suppression of ELMs. In particular, localized stochasticity around the pedestal top has been considered as a key physics mechanism of the RMP ELM suppression and found to reproduce details of the experimental plasma profiles in DIII-D ELM suppression shots [37-39]. In addition, direct experimental observation of the narrow and localized stochastic layer in the edge of KSTAR plasmas with RMP has been reported recently [40]. In order to understand ELM suppression access boundary and relevant physics mechanism, the limit of ELM suppression has been explored across a wide range of critical parameter values (q95, pedestal collisionality, rotation, plasma shape, etc) through multi-year experimental efforts on KSTAR. Recent nonlinear two-fluid and gyrokinetic simulations have also been conducted in a detailed manner to help elucidate the basic physics mechanism of RMP ELM suppression in KSTAR. Meanwhile, real-time 3D control techniques have been developed and tested to maintain ELM suppression in long-pulse RMP scenarios in KSTAR. Considering all the above research progress, this section describes recent highlights of RMP ELM control studies in KSTAR by covering key experiments and physics results, 3D optimization and operating windows, real time 3D control techniques, and nonlinear two-fluid MHD simulation results of RMP ELM suppression.

2.1. Key experiments and physics results

2.1.1. ELM-crash suppression access dependencies on critical physical parameters

The well-separated narrow q_{95} window ($\Delta q_{95} \approx 0.1$) is one of the most characteristic accessibility conditions for RMP ELM suppression although wide q_{95} window of the ELM suppression is highly preferred for stable ITER operation. Here, q_{95} is the magnetic safety factor at 95% of the normalized poloidal magnetic flux. Full ELMs suppression is observed only at specific q_{95} (q_{95}~m/n) by RMPs, where m and n are the poloidal and toroidal mode number. In recent KSTAR experiments, we tried to investigate whether the q95 window can be widened as the RMP current strength increases (Fig. 2). The experiments used typical RMP configuration of n = 1, +90 degree phasing with conventional q_{95} scans around 5 for different RMP current amplitudes. It can be seen that the width of the q95 window is gradually expanded as the RMP current strengths (I_{RMP}) is increased. The highest width of the experimentally observed q95 window is about 0.7 ($\Delta q_{95} \approx 0.7$) at I_{RMP} of 2.65 kA/t as shown in Fig. 2 on the right, which is nearly two times larger than that ($\Delta q_{95} \approx 0.3$) at I_{RMP} of 2.2 kA/t in Fig. 2 on the left. In fact, $\Delta q_{95} \approx 0.7$ corresponds to a very wide width of the q_{95} window, in comparison with the typical width ($\Delta q_{95} \approx 0.1$) observed on multiple devices up to now. The result implies that if there is no risk of mode-locking in core, a sufficiently wide q95 window could be obtained through RMP current amplitude control. Also, it can be noted that the q95 window is expanded asymmetrically around q_{95}~5, i.e., the window width above q_{95}~5 is two times larger than that below q_{95}~5. Remarkably, we find that all these essential features of q_{95} dependence of ELM suppression access window can be well explained by nonlinear MHD modeling results as will be discussed below in section 2.4.1 (see Fig. 15).

As shown in the q_{95} window of RMP-driven ELM-crash suppression in Fig. 2, edge parameters are closely related to the onset of the suppression phase. KSTAR constructs a pedestal parameter database of RMP-driven ELM-crash control experiments to investigate suppression windows [34]. The database includes only datasets from qualified discharges, having reliable profile diagnostics data, such as the Thomson scattering (TS) system (for n_e and T_e) [41] and the charge exchange spectroscopy (CES) system (for T_i and V_{tor}) [42]. The relative error of the estimated value from a fitting process is usually less than 15 % at the pedestal top [34]. All the discharges in the database have the following configurations: $B_T(R_0)$ = 1.8 T, a lower single-null (LSN), and n = 1, +90 degree phasing RMP configuration. The safety factor at 95 % poloidal magnetic flux surface (q_{95}) is ~4.9-5.5 included in q_{95} suppression window. Plasma shape parameters are below; upper triangularity (δ_u) ~ 0.36 ± 0.03, lower triangularity (δ_l) ~ 0.79 ± 0.13, and elongation (κ) ~ 1.74 ± 0.03. During the RMP phase, P_{NBI} ~ 2.8-3.7 MW when the neutral beams are the only auxiliary heating source and otherwise the second harmonic electron cyclotron heating (ECH) is combined with the NBI (P_{ECH} ~ 0.5-1.3 MW and P_{NBI} ~ 1.6-2.1 MW). Within experimentally investigated parameter space so far, the database provides pedestal parameter ranges achieving ELM-crash suppression under n = 1 RMPs. As shown in figure 3(a), most ELM-crash suppression data points are below $n_{e,ped} = 1.5 \times 10^{19}$ m^{-3}. The range of electron pressure (p_e) and normalized electron collisionality ($\nu_e^* = 6.921 \times 10^{-18} Rq_{95}n_eZ_{eff} \ln\Lambda_e/\varepsilon^{3/2}/T^2_e$ [35]) in case of the suppression are $0.2 < \nu_{e,top}^* < 1.1$ and $0.7 < p_{e,top} < 1.9$ kPa, respectively. The ν_e^* range of the suppression is overlapped with that of other tokamaks, such as ASDEX Upgrade ($0.15 < \nu_{e,top}^* < 0.25$) [43] and DIII-D ($\nu_{e,top}^* < 0.5$) [44, 45], but wider [34]. The ELM-crash suppression in high $\nu_{e,top}^*$ in KSTAR is probably due to relatively high toroidal edge rotation compared to other tokamaks. TM1 (nonlinear two-fluid MHD simulation [39, 46]) suggests that the high rotation can lead to the ELM-crash suppression in high ν_e^* (or n_e) by reducing edge $|\omega_{\perp,e}|$. In toroidal rotation speed space, all the ELM-crash suppression points are above $V_{tor,ped}$ > 40 km/s (figure 3(b)), similar to the DIII-D datasets describing rotation threshold of suppression [45, 47], but in contrast to ASDEX Upgrade cases where the suppression is independent on toroidal rotation [48]. Since the outer region covered by data points is not fully explored yet, the pedestal parameter ranges above do not indicate boundaries or thresholds of the RMP-driven ELM-crash suppression window in KSTAR. It is planned to explore the parameter space outside the investigated region, including ITER-relevant pedestal conditions ($\nu_{e,top}^*$ ~ 0.1 and low-torque low-rotation) to confirm the suppression windows. The KSTAR NBI and ECH power upgrade in the future will open the possibility to obtain the ITER-relevant pedestal conditions.

In the Korean fusion demonstration reactor (K-DEMO), target β_N is 2.8-3.2 depending on steady-state scenarios [49]. The RMP-driven ELM-crash suppression plasmas need to satisfy the target β_N of K-DEMO during the suppression phase to contribute to the realization of the fusion reactor. However, the KSTAR ELM-crash suppressed plasmas have not achieved β_N > 2.5 yet. The database above is extended to study parameters affecting β_N and find the recipe for high β_N during the suppression phase. Since the existence and quality of profile diagnostics are not requirements in this analysis, more discharges and data points are included in the database than in the pedestal parameter database. The database includes experiments in both n = 1 and n = 2 RMP configurations. Figure 4 shows the β_N of the ELM-crash suppression phase in different P_{NBI} and I_{RMP}, respectively. The plasmas have different β_N despite the same P_{NBI} or I_{RMP}. The parameters not shown here, such as the pedestal density, current distribution, and plasma shape, can affect the plasma confinement. However, it is a clear trend that β_N becomes high in higher P_{NBI} (figure 4(a)) and lower I_{RMP} (figure 4(b)). A possible approach to achieve the target β_N is applying minimum I_{RMP} triggering the suppression onset with P_{NBI} as high as possible. The future KSTAR campaign will check the accessibility to high β_N conditions during ELM-crash suppression based on the preliminary β_N database analysis.

Plasma shape is another important parameter to determine the accessibility of the ELM suppressed states in tokamaks. Previously, distintive plasma shape dependence of the RMP ELM suppression has been found in KSTAR [50] as well as in ASEDX-Upgrade [51]. Therefore, a dedicated establishment of the RMP-driven, ELM-crash-suppression on ITER-similar shape (ISS) and ITER-like low q_{95} discharges in KSTAR will be of great help to ITER opertaion of the RMP ELM control scheme. Note that the ISS target shows lower triangularity (δ_l) ~ 0.45 and q_{95} ~ 3.2 - 3.4 [52], which are both much smaller than those in typical KSTAR ELM suppression discharges as described above. Although various advanced control techniques were required to build the ISS target in KSTAR, we have actually succeeded in achieving the first RMP ELM suppression on the ISS target by n=2, +90 degrees phasing RMP in KSTAR [52]. Further experimental efforts are being continued to robustly access the ELM suppressed regimes on the ISS target with lowered q_{95} (~ 3.1) in KSTAR, as well as to understand the relevant physics mechanism.

2.1.2. Understanding of ELM control by the ITER-like 3-row versus 2-row RMPs

Taking advantage of ITER-like 3 row in-vessel control coils (IVCC) in KSTAR, KSTAR has explored various combinations of IVCCs in controlling the ELMs. Although the original motivation was to benchmark a feature of typical 2-row RMP-driven, ELM-control in the existing devices with that of ITER-like 3-row counterpart, both similar and dissimilar findings have been tabulated. For example, as long as 2-row RMPs have been turned to be effective in suppressing the ELMs, more or less a lower level of RMP current amplitudes in the 3-row RMPs would be expected to be equally valid. However, in terms of the divertor thermal loading, 3-row RMPs have been much more favorable in reducing the peak of divertor heat flux, as well as in diffusing the thermal load onto a wider area, in comparison with 2-row RMPs [53]. Tentatively, the presence of a third row is likely to diffuse a helical structure that might have been rigidly structured in 3-row RMPs, which is completely missing in a 2-row RMPs. Nonetheless, a future follow-up in terms of modeling needs to be made in quantifying such hypothesis. Also, in a lower-single-null (LSN) plasma, lower two-row RMPs turned out to be much more effective in suppressing the ELMs than upper two-row RMPs [54], as shown in Fig. 5. This result may provide potentially critical information for ITER RMP operation, suggesting that LSN plasmas in ITER would be more effectively ELM-controlled by lower RMPs if 2-row RMPs are planned to be implemented. Interestingly, this result reminds us of a maximal ratio of X-point vs midplane displacement in mitigating the ELMs via RMPs as observed in MAST [55]. To fully understand the relevant detailed physics mechanism, a systematic follow-up study will be conducted in near future, which also includes a quantitative comparison between the experimental and simulation results.

2.1.3. Edge fluctuation & $V_\perp$ dynamics in 3D ELM suppressed vs. ELM-free H-mode plasmas

In the KSTAR, the change of spatial structure and temporal dynamics of ELM and edge turbulence have been investigated to reveal underlying physics using electron cyclotron emission imaging (ECEI) system [56]. To our surprise, we have identified ELM filaments that still maintained, even when the ELM crash has been completely suppressed on H_α signal by $n = 1$ RMP (Fig. 6(a)). Recent nonlinear MHD simulation has succeeded in reproducing the ELM filaments during the ELM suppression phase, which will be explained in detail in Sec. 2.4.2. Correlation analysis among the ECEI channels showed that the RMP would keep enhancing turbulent fluctuations at plasma edge toward the ELM suppression. Cross-phase spectrum and spectral power distribution showed that such edge turbulence has a rather broad dispersion with wide range of wave number ($k_\theta < 1\ \mathrm{cm}^{-1}$) and frequency ($f < 70$ kHz) (Fig. 6(b)). The measured wave number gives the characteristic size of turbulence, which is usually compared to the hybrid Larmor radius $\rho_s = \sqrt{2m_i T_e}/eB$. In this example case, $k_\theta \rho_s < 0.1$ using $\rho_s \approx 0.1$ cm. Kinetic ballooning modes (KBMs), microtearing modes (MTMs), resistive ballooning modes (RBMs), and ion temperature gradient (ITG) modes are of similar size characterized by $k_\theta \rho_s \sim 0.1$. Thus, all of these instability modes are consistent with the observed size of the turbulence at the edge and may need other characteristics to be distinguished between each other. Figure 7 represents the spectral power of the turbulence (30-70 kHz) and ELM (5-30 kHz) with RMP current. This may suggests that the RMP induces the edge turbulence and ELM crashes are suppressed when the edge turbulence level exceeds a certain threshold. Auto-bispectrum calculated by single ECEI channel shows the interaction between ELM and turbulence, especially nonlinear three wave coupling. The opposite trend in the spectral power and nonlinear interaction between ELM and turbulence suggests the turbulent eddies induced by RMP interact with ELM filament and may dissipate the free energy for the ELM growth.

In addition, the direct evidence of perpendicular electron flow ($v_\perp$) bifurcation has been measured at the onset of ELM suppression by tracking the high speed motion of turbulent eddies [57]. The phase-slope calculation between the ECEI channels revealed that ELM crashes are suppressed along with a rapid reduction of $v_\perp$, which synchronizes with the transition into and out of ELM suppression (Fig. 8). The profile change of electron temperature T_e and density n_e before and during the ELM suppression was too small to explain the significant change of $v_\perp$. These observations indicate that the change of $E \times B$ flow ($v_{\mathrm{E\times B}}$) is the main contribution to the $v_\perp$ bifurcation whose magnitude is the smallest value at the pedestal top near the q_{95} rational flux surface during the ELM suppression. The changes in normalized $v_\perp$ show that the effective rational flux surface for the ELM suppression is $\psi_\mathrm{N} \sim 0.95$, and the ELM crashes are suppressed when the $v_\perp$ response is strongly sustained at this location. Therefore, keeping $v_\perp$ to a small value at the q_{95} rational flux surface could play an important role in suppressing ELM crashes, which could have benefited from a strong plasma response to the RMP. Such direct measurement of the turbulence fluctuation and changes of $v_\perp$ will contribute significantly to reveal the underlying physics of RMP-driven ELM suppression.

A similar analysis has been performed on naturally ELM-less plasma, analogous to RMP-driven ELM suppression but without using an external perturbation tool. The ELM-less H-mode plasma such as quiescent H-mode plasma [58] is a promising candidate for achieving $Q > 10$ in ITER and is being studied in many devices, including DIII-D, ASDEX-U, EAST. The ELM-less H-mode plasma is accompanied by benign edge harmonic oscillations (EHOs) [59] near the separatrix. The EHOs had long-wavelength (toroidal mode number, $n \leq 4$) and remained stable during the ELM-less phase, and the ELM crashes rarely occurred at this stage. The observed EHOs sometimes appeared discontinuously and synchronized with quasi-periodic RF ($f \sim 500$ MHz) spikes, providing an enhanced particle transport from the core plasma (Fig. 9). This could avoid an increase in plasma edge pressure and prevent ELM crashes. The bicoherence analysis revealed that there is a strong nonlinear interaction between EHOs, and the nonlinear interaction of EHOs has a significant effect on the ELM structure and dynamics. In addition to the EHOs, rotational shear found to play a significant role in the ELM-less phase. If the rotational shear is sufficiently large enough compared to the typical ELMing H-mode plasma, the ELM crashes disappear and the fluctuation level from the EHO increase, resulting in an intense transport event.

2.2. 3D optimization and predictive model of 3D field operating windows

2.2.1. 3D optimization via edge localized RMP

Unlike cylindrical picture that needs different poloidal harmonics to isolate edge resonance from the core, decoupling edge resonance from the core is not straightforward in tokamak plasmas due to mode coupling and kink mode amplification. This strong coupling can be problematic in RMP ELM suppression, as 3D fields typically drive resonant fields from the core to the edge of tokamak plasmas as the core response can lead to disruptive 3D MHD instabilities such as locked modes. Indeed, RMP ELM suppression using low-n RMP is sometimes impossible or has a very narrow window of safe operation [60]. To expand the safe operation window of ELM suppression, we proposed edge-localized RMPs [17] that would improve the safety of applied fields for easier access to ELM suppression even with the low-n RMP. To localize edge response, we use the resonant field calculated by IPEC [31] and core null space projection matrix [17], $\overleftrightarrow{P}_{c,null}$, to systematically decouple edge resonance from the core that takes into account plasma response to applied fields.

As a working example, we used KSTAR ELM suppression target discharge #18730. The target plasmas are operated with a plasma current (IP) of 0.52 MA, toroidal magnetic field of 1.8 T, The co-IP-directed neutral beam injection (NBI) is injected with the heating of 2.78 MW. The edge localized RMP through the optimization can completely remove the core resonant coupling with zero core resonant field at $\psi_N = 0.62, 0.8$ (q = 2, 3) as shown in Fig. 10. This is a significant reduction from the core resonant field from edge dominant RMP compared in Fig. 10. The edge RMP strength by the edge localized RMP is decreased by 33% from the edge RMP strength of the edge dominant RMP, which is a relatively small penalty considering the strong coupling between the edge and core dominant modes.

Using this method, it is also possible to optimize RMP, using three rows of 3D coils in KSTAR which are located at, below, and above the midplane, and each with 4 coils of roughly 90◦ extents in the toroidal direction. As the power supplies for the 3D coils in KSTAR have the capability to change the coil's current of each row independently to drive n=1 field, i.e. with arbitrary amplitude and toroidal phase of n=1 field, KSTAR has 6D freedom in its coil phase space. This 6D coil phase space, which is virtually 5D in KSTAR due to small intrinsic non-axisymmetry, can be used to apply a flexible poloidal spectrum to optimize RMP coupling. The edge localized RMP space is calculated in this 5D coil phase space to keep the safety and efficiency of ELM suppression [61]. The application of the edge localized RMP (#26015) shown in Fig. 11 can expand the safe operational window of ELM suppression without LMs compared to the conventional 90° phasing (#26014) which is often used to generate the RMP to suppress the edge-localized mode in KSTAR [11,60]. This 3D optimization result shows that the edge-localized RMP can be an efficient way to demonstrate safe ELM suppression in future devices such as ITER as long as multiple arrays of 3D coils are available.

2.2.2. Development and validation of predictive model of 3D field operating windows

A central complexity in validating 3D field physics in tokamaks arises from the many degrees of freedom in generating 3D fields and plasma responses. Machine-machine variations in 3D coil position and density can easily confuse studies without a clear physics basis. Recent progress in KSTAR has potentially provided a resolution, by demonstrating that the variable effects due to 3D field spectrum are mainly the outcomes of ideal response to 3D fields in fast MHD time scales and thus can be well separable as an outer-layer response from inner-layer dynamics in subsequent time scales [17]. The diagram shown in Fig. 12. on the left illustrates three major consequences of n=1 3D fields predicted in KSTAR, including the disruptive locking due to core resonant fields (red), the ELM suppression by edge resonant fields (blue), and no major MHD events other than transport degradation by non-resonant fields (green). It is a 3D stability diagram on the coil configurational space in a special subset (I_{MID}, ϕ_{TM}) with the $I_{TOP} = I_{BOT} = 5kA$, which is the maximum currents allowed in power supplies, and then with the up-down symmetric differential phase (phasing) $\phi_{TM} = \phi_{MB}$. The trajectories including the dynamic paths to reach to the isolated ELM suppression window near the center, (A-C) were deployed based on the predicted diagram before the experiments. This predict-first approach becomes essential when the number of 3D coils increases as it becomes almost impossible to test all the available options of 3D fields. Note that the levels of 3D variability in KSTAR are high enough for one to claim that the predicted scheme should be valid in entire 3D field space in the studied target plasmas.

An important implication of these KSTAR results is that one can reduce the many degrees of freedom in 3D field space into only a few metric variables, such as the resonant field for the core and edge, to the leading order. The edge resonant field δB_{edge} should be strong enough to modify the edge pedestal profiles and thereby ELMs, while the core resonant field δB_{core} must be minimized to avoid major degradation or disruptive MHD responses in particular when the 3D perturbation has the low toroidal mode such as n=1. The 3D field operating windows for ELM suppression can then be predicted once each threshold for the core and edge resonant field can be identified, that is, by $\delta B_{edge}(\vec{I},\vec{\phi}) > \delta B_{edge,Th}$ & $\delta B_{core}(\vec{I},\vec{\phi}) < \delta B_{core,Th}$, to suppress edge MHD instabilities (ELMs) while avoiding disruptive core resonant field penetration (i.e., at q = 2 surface). Here $(\vec{I},\vec{\phi})$ represents the currents and phases for each row of 3D coils in which the degrees of freedom are proportional to the number of the available coils. In the above studies, the ideal perturbed equilibrium code (IPEC) [60] was used to evaluate δB_{edge} and δB_{core} due to the applied 3D coil currents, and the two thresholds were identified empirically from a single operation point $(\vec{I}_0,\vec{\phi}_0)$. The successful validation of the predicted windows indicates that the local thresholds within narrow resonant layers are not affected by the variations in the external 3D configuration $(\vec{I},\vec{\phi})$ and thus can be determined separably from global plasma response outside the layers. This also means that one can optimize the external 3D configuration only by investigating its coupling to δB_{edge} and δB_{core} even without knowing the thresholds. For example, one can design an edge-localized resonant magnetic field (ERMP) [31], which was discussed above in the Sec. 2.2.1, that has a zero coupling to δB_{core} in principle. In practice, however, because of the limited 3D coil capabilities, it is necessary to know the thresholds to predict if the ERMP can actually suppress ELMs.

The concept of a threshold for major MHD events is also proven here to be relevant. A 3D field can induce a bifurcation to large magnetic islands once the resonant component is greater than a threshold, as commonly understood as a field penetration process [62,63]. An assumption is that a field penetration is typically strong enough to change the ELM instabilities when it happens in the edge, and also to drive disruptive locking when it happens in the core. This assumption has been well verified numerically, in particular recently by TM1 simulations [46,64] which will be introduced in detail in Sec. 2.4.1. TM1 offers a reliable prediction of $\delta B_{edge,Th}$ and $\delta B_{core,Th}$ by including various non-ideal physics, which can then be integrated with an ideal response simulation for $\delta B_{edge}(\vec{I},\vec{\phi})$ and $\delta B_{core}(\vec{I},\vec{\phi})$ such as IPEC towards the full predictive capability for 3D ELM suppression windows. It should be emphasized though that the dynamics under 3D ELM suppression is more complicated than just a field penetration process. In the end it is the underlying particle and heat transport with non-linear island evolutions that modifies the profiles, which in turn can induce or change MHD instabilities. In this regard, it is very important to study the impacts of 3D fields to other potential transport mechanisms, such as collisionless neoclassical [65], or turbulent transport [66], as well as to existing MHD instabilities. These issues may ultimately require the full MHD simulation as will be described in Sec. 2.4.2, or gyrokinetic simulation, but the reduced schemes introduced here or in other sections can provide important benchmarking and guidance effectively for such computationally demanding methods.

2.3. Real-time 3D control of ELMs for long pulse

Until now, RMP is conventionally applied in a feed-forward manner. In other words, it is to control ELM-crash by applying RMP to the period where plasma is presumed to exist in ELMing H-mode. However, in plasmas generated under similar conditions as ITER, high-temperature particles and energy caused by a single ELM-crash can damage the plasma-facing components. Therefore, it is necessary to suppress the ELM-crashes completely. For this, the control for ELM-crash suppression should be started from the access time of the H-mode. However, since a physics model that can predict the H-mode transition time occurring at an arbitrary moment has not been established, it is practical to classify the plasma state in real-time using feedback control to suppress ELM-crash. In order to achieve this control in real-time, it is helpful to utilize real-time diagnostic signals such as D_α emission and line-averaged electron density that have characteristic patterns in the H-mode transition. Based on the signals, it is possible to determine the H-mode access time in real-time and apply the RMP before the ELM-crash. Among various methods for real-time classification, we used the Long Short-Term Memory (LSTM) method, which is remarkable for memorizing time series characteristic patterns. The LSTM is a particular type of recurrent neural network among machine learning (ML) techniques. As shown in Fig. 13, a real-time classifier [29] using the LSTM was installed in the KSTAR PCS and receives real-time D_α diagnostic signals and line-averaged electron diagnostic signals to control ELM-crash. In experiments using this ML controller, the result of entirely suppressed the first ELM-crash was obtained. As shown in Fig. 14, the initial ELM-crashes, including the first ELM-crash, were wholly suppressed as RMP was applied based on the judgment of the ML-based classifier right after the H-mode transition. Furthermore, we found that the resulting ELM-free state is usually accompanied by the relatively high-beta plasmas during the whole discharge period, with pedestal width wider than that of usual ELM suppressed discharges without ML-based RMP.

Complementarily, an adaptive ELM control scheme [28] has been developed and successfully tested on KSTAR. The control scheme is adjusting RMP amplitude and/or phasing adaptively in real-time to minimize performance degradation in long-pulse ELM suppressed plasmas. Recently, adaptive ELM controller was successfully implemented to maximize a recovery (~60%) of H_{98} and β_N while maintaining ELM suppression. More detailed results will be discussed elsewhere.

2.4. Nonlinear two-fluid MHD simulations

2.4.1. TM1

Previously, the nonlinear modeling by combining the toroidal ideal MHD code GPEC [67] and the nonlinear two-fluid MHD code TM1 [68,69] has demonstrated agreement with the observations of narrow q_{95} windows to access ELM suppression in DIII-D [64,70]. The model shows that the occurrence of q_{95} windows is the need for resonant surfaces with RMP-driven magnetic islands to be at certain radial positions near the pedestal top in order to prevent the expansion of the H-mode edge gradient region towards destabilization of ELMs [39,46,70]. Further validation of this model by using KSTAR experimental results [11,27,30,71] will enhance the capability of predicting ELM suppression in ITER.

The MHD model combines GPEC and TM1 codes to minimize the difference between the modeling and experiment to obtain quantitative predictions of nonlinear magnetic island formation at the pedestal top of KSTAR discharges. The magnetic boundary condition is obtained from the toroidal ideal MHD plasma response calculations using the GPEC [67]. GPEC uses a kinetic equilibrium before ELM suppression to calculate the total (ideal plasma + vacuum field) response on the TM1 simulation boundary at $\psi_N = 1$, resolved into poloidal harmonics $\delta B_{m,n}$. Here, the ideal plasma response is mainly the edge kink (edge kink-peeling) response, which is thought to be important in ELM suppression. TM1 is a nonlinear time-dependent two-fluid MHD code with cylindrical geometry and circular cross-section. TM1 simulates the bifurcation from screening to penetration of resonant fields in the pedestal by solving the motion equation, and it also self-consistently simulates the particle and thermal transport through the electron continuity equation and the energy transport equation. Physically, RMP enhances parallel collisional transport across the formed magnetic island or screening current, leading to enhanced particle and thermal transport across rational surfaces. The simulated reduction in the pedestal pressure from the MHD model is used to determine the access of ELM suppression.

Based on the plasma parameters of shot 18730, the MHD model is used to predict the q_{95} windows of ELM suppression for $n = 1$ RMP as shown in figure 15(a) represented by the pedestal pressure reduction versus q_{95} and RMP coil current. Here, the predicted RMP strength B_r is converted to RMP coil current utilizing the calculation with GPEC for the target shot 18730. This treatment enables direct comparison between TM1 prediction and the database by using the RMP coil current instead of B_r. The criterion of 15% reduction in pedestal pressure is used according to comparison with DIII-D results [70], as indicated by the blue curves. It is predicted that the $m/n = 4/1$, 5/1 and 6/1 component islands formation at the pedestal top determine the ELM suppression windows at q_{95} around 4, 5 and 6. The q_{95} windows become wider when increasing RMP strength, and the distance between neighboring q_{95} windows is 1. This prediction is consistent with KSTAR experiments, as indicated by the comparison with its ELM suppression database in black circles, all these three q_{95} windows have been observed in the experiment. The MHD model also correctly predicts the q_{95} windows for KSTAR $n = 2$ RMP ELM suppression as shown in figure 15(b). It shows the comparison between TM1 simulation based on shot 18594 and KSTAR $n = 2$ ELM suppression database. Six q_{95} windows determined by 6/2 to 11/2 component RMPs are predicted, and four of them are observed in the KSTAR experiments as indicated by the black circles, they are around 3.3, 3.8, 4.3 and 4.8. The scatter of the experimental database is probably due to the variation in the plasma parameters, for example the change in the pedestal density [64]. Based on the success in predicting the q95 windows of ELM suppression in KSTAR, future work will be performed to validate the mechanism of density pump-out caused by pedestal-foot magnetic island formation, the features of q_{95} windows from the simulations and explore ELM suppression in higher q_{95} high β_p plasma.

2.4.2. JOREK

To improve the understanding of the ELM suppression mechanism, we report the attempt to consider nonlinear RMP physics. Interestingly, the pedestal degradation in the experiment is not sufficient alone to suppress ELMs. While the linear stability of ELM improved owing to the degraded pedestal, it is not a sole contributor to ELM-crash-suppression, in that the coupling between ELM and RMP must participate to non-linearly saturates ELM to suppress mode crashes. The work presented in this paper is performed with the 3D non-linear extended MHD code JOREK [72,73]. 4-field reduced MHD equations [74] are employed to describe the plasma response under the presence of RMPs. Ion and electron temperatures are assumed to be the same. RMP in JOREK simulations is treated with a similar approach as in Ref. [74]. Perturbed poloidal magnetic flux from vacuum RMP calculation is applied as a modified boundary condition in the JOREK computational domain. It is based on the vacuum approximation as the computational domain boundary is far from the main plasma. The perturbed boundary condition is gradually established during 300 Alfven time steps (τ_A). The plasma response after 1000 τ_A is considered as the RMP-driven equilibrium response, where the numerical convergence is achieved. In this way, the penetration of RMP into the plasma is evaluated self-consistently. The simulation includes braginskii-like parallel heat conductivity, experimental-like perpendicular diffusivities, and sources. Note that we use the resistivity 40 times larger than the actual value for numerical reasons.

KSTAR plasma (#18594) [57] is used in this work as a reference case where ELMs are suppressed with n=2 RMP of 90° phasing. The relevant plasma parameters are plasma current ($I_{\mathrm{p}} = 0.66$ MA), stored energy ($W_{\mathrm{MHD}} = 0.43$ MJ), and line average density ($n_{\mathrm{e}} \sim 3.3 \times 10^{19}\ \mathrm{m}^{-3}$). In addition, its main parameters are; toroidal field ($B_{\phi} = 1.8$ T), $q_{95} \sim 4.0$, and global poloidal beta ($\beta_{\mathrm{p}} \sim 1$). Complete ELM suppression is achieved with RMP coil current $I_{\mathrm{RMP}} \sim 3.5$ kA with the degradation of both density and temperature pedestals.

ELMs with toroidal mode numbers of $n \leq 14$ are included in the simulation to study the effect of RMP on ELM stability. Note that $n > 14$ modes are also linearly unstable, and the $n = 12$ mode is the most unstable. Because the growth rate of $n = 10$ is similar to that of $n = 12$ as low n modes are dominant in the nonlinear phase, it is reasonable to exclude $n > 14$ modes to meet the limit of our computing resources. Also, previous numerical modelling [75] revealed that the $n = 2$ structure induced by RMP suppresses the growth of odd modes, and only even modes play a dominant role in the nonlinear phase when RMP is applied. Therefore, n= 2, 4, 6, 8, 10, 12, and 14 harmonics are considered in this study. Nevertheless, one of the important limitations of this study is that only a limited number of even modes are considered. We note that this numerical simulation only considers the interactions between MHD modes. The interaction between ELM and turbulence observed in the experiment will be included in future studies using advanced MHD modeling.

The simulation results for the case with $I_{\mathrm{RMP}} = 4$ kA and without RMPs (natural ELMs) are presented in Fig. 16 (a). For natural ELMs, the total perturbed energy shows bursty behaviour, presented as the red dotted line. When RMPs are applied, ELMs are fully suppressed, where all modes are saturated and remain stationary without any mode crashes [76]. Their saturated value is similar to the initial amplitude imposed by the coupling with the n=2 component. It is noteworthy that ELMs are suppressed in the experiment with $I_{\mathrm{RMP}} = 3.7$ kA, which agrees reasonably well with our modeling results. Interestingly, the ELM structures are still observed in the ELM suppression simulation [Fig. 16 (b)], indicating that ELMs under RMPs are nonlinearly suppressed rather than linearly stabilized. This may explain why edge filament structures are observed during the ELM suppression experiment as discussed in the Sec. 2.1.3 (Fig. 6(a)). Note that the filament structures are spatially locked during the suppression phase in both simulation and experiment.

Suppression of ELMs with the RMPs can be related to the degraded mean pedestal, which is the driving source of ELM instability. It may also result from the increased mode coupling of ELMs ($n > 2$) with RMP-induced plasma response ($n = 2$), which has been found in previous studies [77,78]. To find the reasons for mode suppression, ELM stability is investigated with the degraded mean pedestal profile, while mode coupling of ELM with RMP is excluded. As shown in Fig. 17 (a), the linear growth rate of ELM decreases more than 60% for all n as compared to the case without pedestal degradation. However, ELMs are still non-linearly unstable, and a considerable mode crash occurs despite small growth rates. In Fig. 17 (b), mode saturation is possible only when mode coupling is included. This indicates that the mode coupling has a dominant effect on the ELM suppression of our case rather than the reduced destabilizing source owing to the pedestal degradation.

3. Error field (EF) control

In KSTAR, n=1 intrinsic EF was measured to be as low as $\sim 4 \times 10^{-5} B_0$ even at $\beta_N \sim 2$ [27] which should have significant impacts on several plasma properties such as plasma rotation. It is also important to understand how the EF is projected as β_N is increased (i.e., 2.5, 3, and 3.5), which could help us reach the EF corrected high performance plasmas in KSTAR. In this section, we discuss recent experimental results of intrinsic EF measurements in KSTAR along with a brief explanation of a novel scheme of comprehensive EF correction in tokamaks.

3.1. Intrinsic EF in low versus high beta plasmas in KSTAR

As shown in [27], the n=1 intrinsic EF has been diagnosed at low, intermediate and relatively high beta plasmas, enabling us to recognize a measurable level of intrinsic EF in high beta plasma even in KSTAR. Specifically, the presence of finite n=1 intrinsic EF in high beta plasmas is expected to influence high-performance plasmas that could be readily interacting with neoclassical tearing mode (NTM) or possibly with resistive wall mode (RWM) that is to be seen in a much higher β_N (e.g. > 3) in KSTAR. However, it is to be noted that the n=1 intrinsic EF at low-beta plasmas in KSTAR is unprecedentedly as low as $1 \times 10^{-5} B_0$, and that no routine operational procedure of error field correction (EFC) is implemented yet in the KSTAR. In general, intrinsic EF should be smaller at low-beta plasmas than that at higher-beta ones because it gets larger as β_N is increased due to the resonant field amplification (RFA) effects driven by the least stable ideal MHD mode (e.g. an external kink mode) [79].

In fact, a few different methods of n=1 intrinsic EF measurement have been tested to clarify a finite but elusive level of EFC in fusion plasmas. First, the most well-known method is called 'compass' scan [80], in which a known non-axisymmetric field coil is energized and ramped up until a mode locking occurs. Assuming the onset of the m/n=2/1 mode-locking would be triggered at the same level of magnitude dB, such non-axisymmetric coil current ramp-ups at a few toroidally displaced positions allow us to pin-point the amplitude and phase of n=1 intrinsic error field, whose encircled fit would be measured to be off-centered. According to this compass scan, KSTAR has been diagnosed to possess an extremely low level of n=1 intrinsic error field in low beta plasmas [81]. However, when such compass scan is applied to high beta plasmas (e.g. β_N ~3), the magnetic perturbation has substantially reduced β_N (e.g. ~2), which naturally questions the validity of the measurement. On the other hand, taking advantage of the plasma rotation reduction associated with electromagnetic torque driven by external MP without provoking a mode-locking, a toroidal scan of 'phase-flip' MP at each toroidal phase allows us to locate a specific toroidal phase, where the maximal rotation difference during phase-flip is seen. As expected, this method is less invasive than the compass scan, minimizing the β_N reduction (e.g. 2.5, instead of 2). Nonetheless, the latest measurements of these two methods have poised additional challenges, in that not only the amplitude but also toroidal phase of the measurements are vastly different. Even if the latter is more or less quadratically proportional to the MP, additional experiments and analyses are needed to clarify the intrinsic EF in high-beta plasmas.

3.2. n=1 versus n=2 EF thresholds

In the tokamak, n=1 and n=2 error fields can drive disruptive locked modes (LMs) when their strength exceeds a threshold value. The error field threshold should be understood for safe operation to avoid LMs as tokamak can operate with an intrinsic error field or externally applied resonant magnetic perturbation.

The n=1 and n=2 EF thresholds in KSTAR are investigated by slowly increasing n=1 and n=2 non-axisymmetric magnetic fields using in-vessel control coils (IVCC) as shown in Fig. 18 in KSTAR Ohmic plasmas. The target plasmas are operated with a plasma current of 0.6 MA, toroidal magnetic field of 2.0 T. The growth of the n=1 mode amplitude at t~3.0 s in Fig. 18(d) indicates the penetration of the LM driven by the applied n=1 field and eventually disrupts plasmas. Similarly, the growth of n=2 mode at t~3.6 s in Fig. 18(h) indicates n=2 EF thresholds, where the n=1 grows with n=2 modes even with externally applied n=2 fields. Be aware that n=1 mode growth right after the onset of n= 2 mode is not a universal feature of n=2 penetration in KSTAR as observed at higher density Ohmic plasmas [82].

Both n=1 and n=2 error field thresholds in Ohmic plasmas at different densities are calculated with three different criteria, IPEC resonant field at q=2 (n=1), 3/2 (n=2) surface, overlap field, and vacuum resonant fields as shown in Fig. 19 [82]. For all criteria, the n=2 threshold is lower than the n=1 threshold over the broad density range, unlike a similar level of threshold observed in DIII-D [83]. Meanwhile, the low n=2 error field threshold at high density ($\bar{n}_e > 3\times 10^{19} m^{-3}$) resembles the non-monotonic density dependence observed for the n=1 error field threshold. These results complicate a simple extrapolation of the n=1 to n=2 threshold. The differences can be due to the hollow rotation profiles and the low rotation level near the q=3/2 and q=2 surface in the KSTAR Ohmic plasmas which is different from the typical rotation profile with NBI heating that has higher rotation near the q=3/2 than q= 2 surface as discussed in previous study [82]. Also, a direct comparison of n=2 and n=1 experiments can be difficult as n=2 experiments are done in the different year possibly with a different wall condition. More experiments should be done in the future to understand the different thresholds.

3.3. Quasisymmetric magnetic perturbation (QSMP)

The rotational damping by intrinsic error fields as introduced in Sec. 3.1 is mainly caused by collisionless particle drifts across flux surfaces which is well known as a neoclassical toroidal viscosity (NTV) [65,84] effect. NTV is not as immediately dangerous as locked modes but can eventually affect various instabilities that are dependent on rotation or rotation shear profiles. Another interesting feature is that NTV can be induced not only by resonant error fields but also by non-resonant error fields. Therefore, a need to compensate non-resonant error fields has been well recognized, but it was difficult to properly quantify the compensation due to a number of non-resonant modes and non-linearity of NTV on those modes. Recent progress in KSTAR is nonetheless elucidating a robust path of non-resonant error field correction. The new scheme essentially finds a way to deform tokamak plasmas in the presence of 3D error fields while restoring a quasi-symmetry in particle orbits which in principle should eliminate the fundamental causes of NTV. Such a quasi-symmetric magnetic perturbation (QSMP) has been predictively optimized by general perturbed equilibrium code (GPEC) [67] and successfully tested in KSTAR as well as DIII-D tokamaks [85].

Fig. 20 shows the KSTAR experiment where three distinct types of 3D fields, a QSMP, a non-resonant magnetic perturbation (NRMP) as well as a resonant magnetic perturbation (RMP) were all applied in a single discharge. One can see in comparison that the RMP induced perturbations in all transport channels including density, temperature and rotation, while the NRMP induced only rotational damping. In contrast, the QSMP did not bring any noticeable effect, despite the maximum KSTAR coil currents up to 10kAt. Fig. 20 (d) shows that the GPEC prediction becomes also quantitatively valid, as far as the total integrated torque is concerned. It was also shown in KSTAR experiments that the QSMP is perfectly safe even though transient phases including L-H transitions, where the conventional error field correction (EFC) scheme based on only resonant error fields remained still disruptive in COMPASS and also DIII-D tokamak experiments [85].

A practical implication of these results is that a QSMP indeed encapsulates an ideal and safe form of residual error fields and so can be a new basis for a comprehensive EFC against both resonant and non-resonant error fields. More broadly, these studies illustrate the utility of extending the concept of quasi-symmetry from stellarators [86-87] to a perturbed tokamak, opening a new path for integrated 3D tokamak optimizations. For example, one could leave a beneficial RMP or NRMP for the control of local instabilities while holding quasi-symmetry as much as possible in other locations. Such a more sophisticated 3D optimization would be possible only when the 3D coils are sufficiently flexible, but this work offers important insights on what it would take to minimize unnecessary 3D field effects.

4. 3D field effects on rotation & transport

Applied 3D fields modify 2D nested magnetic surfaces to various complex 3D geometries such as three-dimensionally deformed magnetic flux surfaces, islands, and stochasticity. As a result, non-ambipolar 3D neoclassical dynamics & E_r, MHD, and turbulence modes respond to this change nontrivially, which greatly affects the global particle, energy, and momentum transport of main, impurity, and energetic particles in tokamaks. Some of these problems have been investigated experimentally in KSTAR, such as the detailed 2D measurement of T_e turbulence around the macroscopic isolated island [32], and will be explained below in this section. Particularly interesting would be to understand how the turbulent transport changes during the transition from isolated large island to multiple thin islands or stochastic regimes. In this regard, KSTAR's 2D ECEI system should be a useful tool to probe island and stochastic layer T_e turbulence with high spatial and temporal resolution, which is unprecedented in other tokamaks. Ultimately, the goal here is to use combined experimental and simulation results to predict quantitatively the global confinement in terms of various transport channels in plasmas with 3D fields for KSTAR in the near future, and ITER and K-DEMO finally.

4.1. 3D effects on energy confinement and toroidal Alfven eigenmodes (TAEs)

There are a number of experimental observations in KSTAR that demonstrate the effects of toroidal rotation braking driven by 3D magnetic field, which is called magnetic braking, on the confinement and transport [88, 89]. One recent observation is the confinement improvement achieved in the magnetic braking experiment that investigated confinement characteristics of slow rotating neutral beam heated plasmas, which is not a typical 3D field effect on the confinement. A typical discharge is shown in Fig. 21 (a), where the n = 1, 0-degree phasing 3D field was applied to the neutral beam heated H-mode plasma. Rotation reduction and modification of rotational shear by magnetic braking in the whole plasma volume was observed. Interestingly, the plasma stored energy was increased by up to 15-20% in spite of density pump-out, which was accompanied by enhancement of fast ion confinement represented by increase of neutron rates. The improved thermal confinement in such discharges was identified by the enhanced pedestal, leading to increase of the core ion temperature. Turbulent fluctuation inside the pedestal was found to be reduced during the improved confinement phase under 3D magnetic field, implying the correlation between reduced toroidal rotation by magnetic braking and turbulent transport reduction. Mitigation of the ELMs was observed during the improved confinement phase, which further benefit the potential application of the 3D magnetic field for high performance tokamak operation.

Another interesting example of the 3D magnetic field effect is the modification of the Alfvenic activities. It has been reported that resonant 3D magnetic field mitigated and/or suppressed the global

Alfven eigenmodes (GAEs) in the NSTX [90] and the toroidal Alfven eigenmodes (TAEs) in the ASDEX-Upgrade experiment [91]. These results claimed that the 3D field induced fast ion losses modify the fast ion distribution and thereby the fast ion drive of the AEs, leading to mitigation and/or suppression of the AE activities. While the resonant 3D field has been found to enhance fast ion losses [92], its impacts on the AE stability has not yet clearly identified in KSTAR. On the other hand, destabilization of the TAEs has been observed in the non-resonant magnetic braking experiment on KSTAR [93]. In this experiment, it was pointed out that the TAEs can be destabilized by 3D magnetic field induced toroidal rotation braking. The TAEs were destabilized by significant reduction of the toroidal plasma rotation with near-zero rotational shear driven by the magnetic braking. The TAE frequencies predicted by ideal stability analysis with the reduced toroidal rotation were in good agreement with the measured mode frequencies. These analyses indicated that the TAE stability is strongly correlated to the reform of the Alfven continuum, which is caused by modification of the rotation and rotational shear profile in the presence of 3D magnetic field. Fig. 21 (b) presents a recent magnetic braking discharge, showing the TAE mode activities that respond to the magnetic braking and the electron cyclotron heating. One can find from this discharge that the 3D magnetic field modified the TAE mode structure and frequencies, while the ECH activated new modes of n = 2 ~ 4. The modifications in the AE stability are caused by reform of the Alfven continuum due to modifications of rotation and safety factor profiles by the 3D field and ECH. Such observations indicate that the 3D magnetic braking can change the AE stabilities and the associated fast ion transport, which motivates the utilization of 3D magnetic braking for control of the AEs in the future experiment. One notes that the fast ion losses driven by the 3D magnetic field should be taken into account for design of the AE control experiment to optimize the fast ion confinement.

4.2. Plasma rotation alteration induced by 3D neoclassical transport effects

The 3D fields in a tokamak can change plasma rotation due to the 3D neoclassical transport known as NTV [65,94]. The NTV transport, which is a net radial current, is typically dominated by ions as they collide less frequently and thus drift farther than electrons. This ion NTV typically slows rotation down against the direction of plasma current I_p towards its offset [95]. A recent KSTAR experiment shows the co-I_p acceleration of plasma rotation due to electron 3D neoclassical transport on the top of resistive field penetration and amplified 3D response [96].

The target plasmas in KSTAR are heated by the co-I_p-directed neutral beam injection (NBI) with the I_p= 0.6 MA and the toroidal field B_T =2 T. The discharges #19117 and #19118 in Fig. 22 show a slow but clearly decreasing rotation by the 3D field (magnetic braking), where the initial rotation was higher than the saturation level due to the slightly higher NBI power. On the other hand, the other discharge #19115 in Fig. 22 shows the acceleration of toroidal rotation up to 50 krad/s due to a 3D field (magnetic acceleration). Note that the density and the temperature of thermal species are almost stationary under the RMP unlike earlier studies on electron NTV. Figure 22 also shows that the magnetic acceleration can improve the tolerance of the low-torque plasmas against LMs locking in #19115 as seen by higher tolerance of LM thresholds as indicated by mode locking at higher current even with a low initial injection torque.

A qualitative neoclassical offset estimation and rotation profile evolution of #19115 in Fig. 23 (a) shows that the acceleration and its offset can be explained with an electron NTV rather than by ion NTV. Furthermore, Fig. 23 (b) shows that the measured NTV torque in the experiments can be quantitatively explained with kinetic electron NTV simulation, MARS-K [97,98], which is self-consistent with a hybrid-MHD plasma response where the hybrid-MHD plasma response is validated by ECEI in KSTAR

[96]. Note that the simulation curve in Fig. 23 (b) is obtained by gradually changing T_i/T_e because T_i can simulate the possible torque variations determined by the competition between the collisionless electrons and collisional ions [96]. These KSTAR results show that the electron NTV can be an outstanding mechanism dominating ion NTV and can be utilized to accelerate plasma rotation with a theoretical prediction.

4.3. Energetic particle (EP) loss under 3D field

Degraded fast ion confinement has unfavorable effects on heating efficiency and heat loading on the plasma facing components. Fast ions produced by NBI or fusion product particles act as fuel for plasma heating. Therefore, loss of fast ions should increase heating cost for fusion energy production. It has been consistently observed that externally driven 3D magnetic field perturbation in ELM controlled H-mode plasmas increases fast ion losses. Many experiments on major tokamaks including KSTAR [99], ASDEX-Upgrade [100], DIII-D [101], MAST [102], and EAST [103], have reported such an enhanced fast ion transport using scintillator-based fast ion loss detector. Thus, physical mechanism of fast ion transport due to 3D field must be elucidated to find an optimal way to control fast ions transport.

Practical concern of fast ion loss by 3D field in KSTAR is excessive heat load on the plasma facing components, i.e. poloidal limiters (PLs) in the SOL region [104], though heating efficiency is also a key concern of fast ion confinement study. Heat load on PLs in diverted plasma is mainly contributed by the fast-ions having large drift, not by thermal ions [105,106]. Thus, extra temperature increase of poloidal limiters compared with normal 3D field free operation is mostly due to fast ion loss by RMP as shown in Fig. 24.

To reduce the heat load on the PLs, the experiment in Fig. 24 tried to control the fast ion loss by 3D field rotation accomplished by IVCC coil current phase. Toroidal phase rotation of 3D field caused the temperature of PLs to oscillate in time though temperature during 3D field working time increases. That implies that the fast ion loss depends on the configuration of 3D field and can be localized toroidally [104].

To investigate physical mechanism of fast ion loss due to 3D field, fast ion loss detector (FILD) has been installed in KSTAR near the passive plate [99]. It can measure the energy and pitch-angle of detected fast ions. FILD shows that fast ions having undetectable energies and pitch-angles without 3D field are observed during the 3D field operation. This results along with simulational efforts [104] supports that violation of the toroidal angular canonical momentum conservation drives fast ion drift to the PLs. FILD measurements of fast-ion loss also allow quantitative comparison of toroidal localization of fast ion loss. This quantification makes possible direct comparison with simulation as shown in Fig. 25.

Simulation codes for fast ion of NBI have been developed [92,106]. Two codes are categorized by Full orbit simulation [92] and guiding center following simulation [106]. Both codes calculate the magnetic field at a particle's position by summing of equilibrium and 3D perturbation field. Perturbation magnetic field is calculated including plasma response of external perturbation field [60].

Full orbit (not guiding center orbit) simulation code demonstrated that magnetic field perturbation considering plasma response can reproduce the saturation and threshold observed in KSTAR [89]. This simulation code reveals that break of toroidal canonical momentum cause the enhanced particle transport. Fast ions having low and intermediate pitches ($0<v/v_{\|}<0.8$) experience large oscillation in toroidal canonical momentum space. But for particles having large pitches ($v/v_{\|}>0.8$) oscillate in limited amount.

Perturbation of vacuum field (not including plasma response) cannot reproduce the threshold phenomena. Plasma response amplify the magnetic perturbation in the resonance flux surfaces inside the plasma [60]. Thus vacuum approximation solely does not implement strong perturbation in the plasma region. This difference causes the nonlinear phenomena.

Guiding center following code investigates the case of intentionally misaligned RMP situation showing decrease of fast ion loss with increase of misalignment [104]. In the simulation result, toroidal rotation can rotate peak heat load on the plasma facing components, i.e. PLs. It successfully reproduces the toroidal loss pattern of fast ions detected by the FILD probe as shown in the Fig. 25. [104]

Further works of 3D field effects on the fast ion confinement in KSTAR is progressing in experiments and simulation. Toroidal localization of fast ion heat load by 3D field optimization will be tried to achieve ELM-free long pulse operation, which is one of the main missions of KSTAR. More detailed numerical investigation of fast ion loss mechanism of low pitch angle is conducted to find efficient 3D field configuration. Combination of TRASNP and fast ion transport probability distribution function tries to study fast ion confinement due to 3D field. Fast ion distribution observed by FIDA will be compared with the simulation results.

4.4. Interaction between magnetic island and turbulence

Penetration of 3D field breaks up the nested magnetic flux surfaces of plasmas and opens up a magnetic island at the resonant rational surface [107,108]. The magnetic island is known to be either a fast radial transport channel through the stochastic region formed along the island separatrix [108] or a transport barrier by increasing the flow shear near its separatrix [109,110]. In order to study further the transport characteristics of plasmas with a magnetic island, plasma turbulence around the island has been measured and analyzed [111]. It was found that the interaction between magnetic islands and turbulence makes the transport around the island complicated. Results of the KSTAR experiments on how a magnetic island perturbs plasma turbulence [32] and complex turbulence phenomena which can affect the island evolution will be summarized below [112].

Detailed 2D measurements of plasma turbulence (drift wave instabilities driven by the pressure gradient) around a magnetic island could be obtained by the ECEI diagnostics on the KSTAR tokamak [113]. It showed that plasma turbulence becomes strongly inhomogeneous around the island [32]. Figure 26(a) shows the relative change of temperature fluctuation power before and after the growth of the m=2 magnetic island whose separatrix is indicated by purple dashed lines. The large increase of the fluctuation power was observed outside of the island near the X-point (the field line reconnection site), while the fluctuation power was insignificant all around the O-point (the center of the island). The absence of the significant fluctuation power inside the island could be understood as a result of the flattened pressure profile due to the fast parallel transport along the reconnected field line of the island. The insignificant fluctuation outside of the island at the O-point angle was explained by the development of the strongly sheared flow profile (shown in figure 26(b)) around the island. In particular, the flow shear increases toward the O-point angle. The strong flow shear outside the island at the O-point angle can be responsible for the suppression of plasma turbulence there as shown in the gyrokinetic simulation [33]. The combined effect of the pressure and flow profiles modification by the magnetic island produces a strongly inhomogeneous turbulence around the island.

On the other hand, the complex turbulence phenomena which can affect the island evolution (and so its direct effect on the transport) were also observed [112]. For example, figure 27(a) shows the fluctuation power change before and after the turbulence spreading phenomenon [114]. The fluctuation power decreases in the inner outside and increases in the inside of the island. The sufficiently enhanced turbulence in the inner outside of the island near the X-point could overcome the flow shear at the island separatrix and spread into the island. This nonlocal turbulence spreading is different from the local change of turbulence such that it carries the heat flux [112]. The temperature at the inner outside region decreases with the fluctuation decrease by turbulence spreading, while the temperature increases when the fluctuation is suppressed locally due to the flow shear increase. The accompanying heat influx into the magnetic island could reproduce the pressure gradient inside the island, which could be beneficial for the recovery of the bootstrap current loss and the island stabilization. An opposite harmful contribution of turbulence was also found during the magnetic island driven plasma disruption [112]. Figure 27(b) shows the fast minor disruption driven by the locked magnetic island. A correlated increase of the fluctuation power near the island X-point (the reconnection site) was observed. Note that the similar minor disruptions occur for a much longer time without the significant fluctuation power at the X-point. This observation implies that the fast magnetic reconnection could be facilitated with the more turbulent reconnection site, although it is not the sole mechanism of the fast disruption [115].

5. 3D field effects on divertor heat flux

Since most of the plasma exhaust energy in the steady-state will be localized to a narrow region on the divertor targets, control of the heat fluxes onto the divertor targets is one of the most important concerns for burning-plasma devices such as ITER. Even in KSTAR, as the plasma performance significantly improves, it has become more critical to reduce the divertor heat flux because it can prevent KSTAR from achieving the long-pulse (> 300 secs) plasma discharge while avoiding any possible damage of the divertor target tiles. In terms of the divertor heat flux control, the peak heat flux onto the divertor target is the most important parameters that should be reduced below a certain engineering limit. For example, in ITER, the steady-state divertor peak heat flux should be controlled below ~ 20 MW/m^2. When the 3D field is applied to obtain ELM suppression, it also has a significant impact on the divertor heat flux. In order to assess the alteration of the divertor heat flux during 3D ELM suppression in ITER and beyond, thus, it is required to understand the fundamental relation between the divertor target heat flux characteristics and the applied 3D fields.

In general, as shown in Fig. 28, the peak heat flux onto the divertor target is determined by the plasma operating condition and divertor geometry. The heat flux onto the divertor target comes from the plasma energy entering the scrape-off-layer (SOL) region (P_{SOL}), which is the same with the plasma heating power into the plasma (P_{heat}) – the plasma energy lost by the radiation ($f_{rad}^{core} P_{heat}$). Assuming P_{SOL} is coming to both inner and outer targets by 1:1, the outer divertor target heat flux is mainly determined by the target wetted area (A_{wet}) and can be expressed by the following equation:

$$\hat{q}_{\perp} = \frac{\left(1 - f_{rad}^{div}\right) \cdot \left(1 - f_{rad}^{core}\right) \cdot P_{heat} \cdot \sin\beta}{4\pi R_t \cdot \lambda_q \cdot f_x}, \qquad (1)$$

where f_{rad}^{div} is the fraction of the radiation loss at the divertor region, β is the inclination angle between the striking point and the divertor target, R_t is the major radius of the target, λ_q is the power decay length of the heat flux and f_x is the flux expansion.

Actually, all parameters involved in Eq. (1) are known to be determined by the plasma size or operating parameters. In other words, the peak heat flux cannot be controlled unless we can control the divertor radiation fraction or the effective target wetted area. The divertor radiation fraction can be increased by injecting the certain impurities into the divertor region. As the radiation increases by the impurity, the divertor peak heat flux can be significantly decreased. However, the injection of impurity can degrade the plasma performance significantly or lead to the disruption by increasing the radiation loss of the core plasma while penetrating into the plasma. On the one hand, the application of magnetic perturbations (MPs), which is actively used to suppress ELMs in many tokamaks, has been expected to reduce the steady-state divertor peak heat flux by increasing the effective target wetted area. It is typically expected that the application of MPs can broaden the divertor heat flux profile as it changes the magnetic field topology at the plasma boundary region as shown in Fig. 29.

Recently, KSTAR has clearly demonstrated that the divertor heat flux profile shape is determined by the configuration of MPs as shown in Fig. 30. It was realized that the divertor heat flux profile is clearly split showing the pattern likely what is expected by the EMC3-EIRENE calculation.

However, it has been found that the outer target peak heat flux usually becomes much higher during the ELM-suppression regime than that without RMPs as shown in Fig. 31. This observation contradicts the expectation from the EMC3-EIRENE calculation that usually predicts that the peak heat flux is significantly reduced under the application of RMPs. It may mean that the application of MPs does not change only the target wetted area but also the loaded power onto the target. Recently, a preliminary JOREK simulation result has implied that the loaded powers onto the inner and outer targets can be significantly changed, which lead to more outer target power load, under the application of MPs in KSTAR [116]. The underlying physics on the significant increase of the outer target heat flux by the application of MPs is still under the investigation.

6. Future research plan of 3D field physics toward ITER and K-DEMO

Burning plasmas in ITER and K-DEMO are expected to have several distinctive features: low rotation, low collisionality, high density, comparable ion and electron temperatures due to dominant electron heating, and a dissipative, partially detached state near tungsten divertor. Despite a clear limitation of KSTAR in emulating these burning plasma conditions in the existing capabilities, divertor, heating, and current drive upgrades planned for KSTAR in the near future [24,25] would allow us to access to more ITER- and DEMO-like plasmas than had been achieved so far. More specifically, until 2023, KSTAR will complete its upgrade plan with tungsten divertor and have a total of 24 MW heating powers from NBI (total power up to ~12 MW), ECH (total power up to ~6 MW), ICRF (total power up to ~2 MW), and LHCD/HCD (total power up to ~4 MW). This would provide the capability to address various 3D physics issues relevant to ITER, for example, in ECH/RF-dominated H-modes with low input torque with tungsten divertor in KSTAR that had never been thoroughly explored so far. Therefore, utilizing these favorable ITER-like plasmas as well as state-of-the-art numerical simulations, and diagnostic capabilities, we plan to focus on resolving various critical issues for ITER 3D field physics, as tabulated in the ITER Research Plan (IRP) report [117], until the beginning of ITER full operation phase (~2030). On the other hand, we are also envisioning K-DEMO to use 3D field coils for robust and simultaneous control of ELM, EF, MHD, rotation, transport, and divertor heat flux in high beta plasma operation. Note that high beta ($\beta_N \sim 3.5$) advanced tokamak operation mode is a basic requirement for K-DEMO due to an economical efficiency, while a relatively smaller value of beta ($\beta_N \sim 1.8$) is targeted in the ITER baseline operation phase. Currently, it is expected that KSTAR would contribute to developing stationary high beta plasma operation scenarios for K-DEMO during 2025-2035, while a steady-state long pulse high T_i operation (~300 sec) will be vigorously pursued by 2025. Future research themes of 3D field physics will be briefly explained below.

6.1. Supporting ITER in resolving critical 'ITER urgent issues'

Understanding of the fundamental role the turbulence plays in RMP ELM suppression: Although there have been a lot of new discoveries to understand the physics mechanism of the RMP ELM suppression, the key details in terms of RMP ELM suppression physics need to be further clarified. For instance, turbulence fluctuation was generally observed to be significantly enhanced in RMP plasmas [56,118], but we have not fully understood what kind of role the turbulence enhancement by RMP plays on the onset of the ELM-suppressed states, including the causality among turbulence, resonant field penetration, and ELM suppression. Thus, a more comprehensive study on various effects of turbulence in RMP ELM suppression is one of the top priorities in the 3D physics research plan in the near future.

Validation and prediction of RMP ELM control scheme in ITER-like low rotation plasma with tungsten divertor: Because the input torque from heating and current drive systems in ITER is low, the application of external 3D field may not only drive significant slowing down of plasma rotation and mode locking, but also can make it difficult to achieve robust RMP ELM suppression, as had been reported from DIII-D [45,47]. Moreover, the plasma response to externally applied 3D fields in ITER may not be the same as what we used to see presently in high rotation plasmas, while tungsten accumulation in ELM controlled regimes should be avoided in core. In order to overcome all these uncertainties of the planned RMP ELM control scheme in ITER, we have been addressing various operational challenges within the limits of available ITER-like low rotation plasma in KSTAR. The obtained experimental results will also be used to optimize the applied 3D fields (i.e., with respect to minimum rotation braking, largest plasma response, and maximum impurity exhaust), and assess the relevant RMP ELM control scheme in ITER Fusion Power Operation (FPO) phase [117].

Predictive capability of plasma confinement, impurity, and energetic particle losses under 3D field: A main issue here is to determine the physics basis for the effects of 3D fields on energy and particle confinement, impurity (W) exhaust, and fast particle losses in ELM suppressed regimes in the ITER tokamak and its optimization. In fact, the relevant diagnostic systems to measure impurity and fast particle losses will be expanded and/or newly installed into the KSTAR, as well as the improvement of existing 2D/3D imaging diagnostic system to measure high-resolution turbulent fluctuations (i.e., $\delta n_e, \delta T_e, ...$) simultaneously at the same space and time point. Thus, we are planning to conduct dedicated experiments on KSTAR using high spatial/time resolution upgraded diagnostic system, and thereby validate fundamental 3D transport physics. In particular, we are hoping to benchmark gyrokinetic turbulence simulation results much more accurately than achieved so far, and quantitatively predict the consequences for energy and particle confinement in the presence of 3D fields in ITER.

Control of divertor heat flux and detachment via 3D field and impurity injection: Although the above two tasks would provide optimal RMP scenarios for stable access to ELM suppression with minimized impact on plasma performance in ITER-like plasmas, these scenarios should eventually be compatible with the detached divertor regime with lowered heat and particle fluxes as required for ITER. Exploiting a long pulse capability of the KSTAR tokamak as well as ITER-like three-row in-vessel control coils, we aim at finding the optimized RMP scenarios/phasings that can lower divertor heat load peaks in a (partially) detached divertor regime in order to sustain both ELM suppression and good core confinement stably in long-pulse H-modes. Dedicated experiments on KSTAR will be conducted to articulate how the 3D ELM suppression is correlated with the spatial structure and magnitude of the divertor heat and particle fluxes, and to elucidate the effects of 3D fields on detached divertor operation, as well as to enhance the physics understanding.

6.2. Robust 3D field control of K-DEMO high beta scenarios

Demonstration of a long pulse operation of ELM suppressed high beta plasmas in KSTAR: Because K-DEMO will be a long-pulse high performance plasma, we will first try to demonstrate a long pulse (~100 s) operation of ELM suppressed high beta ($\beta_N > 2.5$) plasmas in KSTAR in the near future before beginning a systematic study on the optimized 3D control of K-DEMO high beta scenarios. For this purpose, various real-time 3D control and optimization techniques will be utilized extensively, such as 3D field optimization via edge localized RMP [31], adaptive ELM control [28] and machine learning algorithm [29], to sustain ELM suppressed high beta plasmas robustly in a long pulse H-mode discharge.

Optimization of K-DEMO high beta scenarios through the use of ex-vessel 3D field coils: While in-vessel 3D field coils are used in ITER, ex-vessel 3D coils are currently being considered as important actuators for high performance reactor scenarios in K-DEMO. Primarily, that is due to the technical challenge of designing internal in-vessel 3D field coils that may not withstand the large neutron fluence inside the vacuum vessel of future reactors like K-DEMO. Low-n ex-vessel 3D coils will be designed [119] to produce an optimal spectrum for controlling ELMs, core MHD, rotation, transport, and divertor heat flux simultaneously in K-DEMO high beta scenarios, similar to what the current KSTAR has. Certainly, we plan to use an ex-vessel 3D coil actuator efficiently to reach the target performance (β_N~3.5) of K-DEMO high beta scenarios, while suppressing the ELM-crashes successfully for long pulse.

7. Conclusion

For nearly a decade of years, KSTAR research has made significant progress in RMP ELM control, EF control, rotation and transport studies under 3D field, and 3D field effects on divertor heat flux and detachment. Recent highlights of KSTAR 3D field studies have been briefly discussed: 1) Narrow and localized stochastic layer around the pedestal top in the edge of KSTAR plasmas with RMP has been identified experimentally, demonstrating the importance of the stochastic layer formation in the RMP ELM suppression process; 2) ELM suppression window has been investigated systematically across a wide range of pedestal parameters (q_{95}, collisionality, rotation, plasma shape, etc). In particular, the q_{95} window of n=1 RMP-driven ELM suppression has been found to be expanded as the RMP amplitude gets larger, which is consistent with the prediction by TM1 simulation; 3) Characteristics of ITER-like 3-row RMPs have been clarified in terms of both ELM control and divertor thermal loading, in comparison with 2-row RMPs. Moreover, up/down poloidal asymmetric coupling in 3-row configuration was confirmed for RMP-driven, ELM-crash suppression in lower-single-null (LSN) plasmas; 4) Real-time 3D control techniques (ML and adaptive ELM control) have been developed and demonstrated successfully for long pulse. In particular, the first ELM can be automatically suppressed in a preemptive manner by ML algorithm; 5) Along with optimized design of an edge-localized RMP and TM1 calculation of the thresholds, predict-first model of 3D field operating windows has been developed and validated successfully; 6) Intrinsic EF and EF thresholds have been diagnosed and analyzed, and a robust and alternative path of error field correction problems in tokamaks (QSMP) was newly devised and successfully tested in KSTAR as well as DIII-D tokamaks; 7) Detailed 2D measurements of plasma turbulence around a magnetic island have been obtained, which showed that plasma turbulence becomes strongly inhomogeneous around the island. Also, turbulence spreading around magnetic island was observed to significantly affect the magnetic island evolution. It should be emphasized that all these remarkable 3D field results could not have been obtained if the relevant unique capabilities of the KSTAR tokamak had not been exploited effectively. In the future research, KSTAR will concentrate on a series of unresolved 3D physics topics directly relevant to ITER as well as exploring a long pulse high performance plasma without ELM crashes to support K-DEMO. Such 3D field research will be further supported by the timely upgrade of the heating, current drive, and tungsten divertor systems in the near future.

ACKNOWLEDGEMENT

The authors would like to acknowledge the hard work of the entire KSTAR team to support 3D field research in KSTAR. This work was supported by Ministry of Science and ICT under KFE R&D Program of "KSTAR Experimental Collaboration and Fusion Plasma Research (KFE-EN2101-12)".

REFERENCES

[1] K. Ikeda, Nucl. Fusion **47**, S1 (2007).
[2] K. Kim *et al.*, Fusion Eng. Des. **88**, 488 (2013).
[3] B. V. Chirikov, Phys. Rep. **52**, 265 (1979).
[4] A. J. Lichtenberg and M. A. Lieberman, *Regular and Chaotic Dynamics*, 2nd ed. (Springer-Verlag, New York, 1992), pp. 1-692.
[5] F. L. Waelbroeck, Nucl. Fusion **49**, 104025 (2009).
[6] J. D. Callen, Nucl. Fusion **51**, 094026 (2011).
[7] J.-K. Park, M. J. Schaffer, J. E. Menard, and A. H. Boozer, Phys. Rev. Lett. **99**, 195003 (2007).
[8] T. E. Evans *et al.*, Nature Physics **2**, 419 (2006).
[9] T. E. Evans, Plasma Phys. Control. Fusion **57**, 123001 (2015).
[10] T. E. Evans *et al.*, Phys. Rev. Lett. **92**, 235003 (2004).
[11] Y. M. Jeon *et al.*, Phys. Rev. Lett. **109**, 035004 (2012).
[12] Y. Sun *et al.*, Phys. Rev. Lett. **117**, 115001 (2016).
[13] W. Suttrop *et al.*, Plasma Phys. Control. Fusion **59**, 014049 (2017).
[14] H. Zhom, Plasma Phys. Control. Fusion **38**, 105 (1996).
[15] P. B. Snyder *et al.*, Phys. Plasmas **9**, 2037 (2002).
[16] A. Loarte *et al.*, Nucl. Fusion **54**, 033007 (2014).
[17] J.-K. Park *et al.*, Nature Physics **14**, 1223 (2018).
[18] A. B. Rechester and M. N. Rosenbluth, Phys. Rev. Lett. **40**, 38 (1978).
[19] L. Cui *et al.*, Nucl. Fusion **57**, 116030 (2017).
[20] O. Schmitz *et al.*, Nucl. Fusion **56**, 106011 (2016).
[21] H. Frerichs *et al.*, Phys. Rev. Lett. **125**, 155001 (2020).
[22] G. S. Lee *et al.*, Nucl. Fusion **40**, 575 (2000).
[23] Y. K. Oh *et al.*, Fusion Eng. Des. **84**, 344 (2009).
[24] Y. K. Oh *et al.*, J. Korean Phys. Soc. **73**, 712 (2018).
[25] H. K. Park *et al.*, Nucl. Fusion **59**, 112020 (2019).
[26] J. Kim *et al.*, Nucl. Fusion **57**, 022001 (2017).
[27] Y. In *et al.*, Nucl. Fusion **57**, 116054 (2017).

[28] F. Laggner *et al*., Nucl. Fusion **60**, 076004 (2020).
[29] G. W. Shin, J.-W. Juhn, G. I. Kwon, S.-H. Hahn, Fusion Eng. Des. **157**, 111634 (2020).
[30] Y. In *et al*., Nucl. Fusion **59**, 126045 (2019).
[31] S. M. Yang *et al*., Nucl. Fusion **60**, 096023 (2020).
[32] M. J. Choi *et al*., Nucl. Fusion **57**, 126058 (2017).
[33] J.-M. Kwon *et al*., Phys. Plasmas **25**, 052506 (2018).
[34] M. Kim *et al*., Phys. Plasmas **27**, 112501 (2020).
[35] O. Sauter, C. Angioni, and Y. R. Lin-Liu, Phys. Plasmas **6**, 2834 (1999).
[36] F. Troyon, R. Gruber, H. Saurenmann, S. Semenzato, S. Succi, Plasma Phys. Control. Fusion **26**, 209 (1984).
[37] G. Park, C. S. Chang, I. Joseph, and R. A. Moyer, Phys. Plasmas **17**, 102503 (2010).
[38] P. B. Snyder *et al*., Phys. Plasmas **19**, 056115 (2012).
[39] Q. M. Hu *et al*., Nucl. Fusion **60**, 076001 (2020).
[40] M. J. Choi *et al*., arXiv:2101.10733 (2021).
[41] J. H. Lee, S. T. Oh, and H. M. Wi, Rev. Sci. Instrum. **81**, 10D528 (2010).
[42] W.-H. Ko, H. H. Lee, D. Seo, and M. Kwon, Rev. Sci. Instrum. **81**, 10D740 (2010).
[43] W. Suttrop *et al*., Phys. Rev. Lett. **106**, 225004 (2011).
[44] T. Petrie *et al*., Nucl. Fusion **51**, 073003 (2011).
[45] C. Paz-Soldan, *et al*., Nucl. Fusion **59**, 056012 (2019).
[46] Q. M. Hu *et al*., Phys. Plasmas **26**, 120702 (2019).
[47] R. A. Moyer *et al*., Phys. Plasmas **24**, 102501 (2017).
[48] W. Suttrop *et al*., Nucl. Fusion **58**, 096031 (2018).
[49] J. S. Kang *et al*., Nucl. Fusion **57**, 126034 (2017).
[50] Y. M. Jeon *et al*., in *27th IAEA Fusion Energy Conference* (Gandhinagar, India, Oct. 2018).
[51] R. Nazikian *et al*., in *26th IAEA Fusion Energy Conference* (Kyoto, Japan, Oct. 2016).
[52] S.-H. Hahn *et al*., Nucl. Fusion in press.
[53] Y. In *et al*., to be published (2021).
[54] Y. In *et al*., in *28th IAEA Fusion Energy Conference* (Virtual Event, May 2021).
[55] A. Kirk *et al*., Nucl. Fusion **55** (2015) 043011.
[56] J. Lee *et al*., Phys. Rev. Lett. **117**, 075001 (2016).
[57] J. Lee *et al*., Nucl. Fusion **59**, 066033 (2019).
[58] K. H. Burrell *et al*., Plasma Phys. Control. Fusion **44**, A253 (2002).
[59] X. Chen *et al*., Nucl. Fusion **57**, 086008 (2017).
[60] J.-K. Park, A. H. Boozer, and A. H. Glasser, Phys. Plasmas **14**, 052110 (2007).
[61] S. M. Yang *et al*., to be submitted (2021).
[62] R. Fitzpatrick, Phys. Fluids **B 3**, 644 (1991).
[63] R. Fitzpatrick, Phys. Plasmas **25**, 042503 (2018).
[64] Q. M. Hu *et al*., Phys. Plasmas **28**, 052505 (2021).
[65] J.-K. Park, A. H. Boozer, and J. E. Menard, Phys. Rev. Lett. **102**, 065002 (2009).
[66] G. J. Choi and T. S. Hahm, Nucl. Fusion **58**, 026001 (2018).
[67] J.-K. Park and N. C. Logan, Phys. Plasmas **24**, 032505 (2017).
[68] Q. Yu, S. Günter, and B. D. Scott, Phys. Plasmas **10**, 797 (2003).
[69] Q. Yu and S. Günter, Nucl. Fusion **51**, 073030 (2011).
[70] Q. M. Hu *et al*., Phys. Rev. Lett. **125**, 045001 (2020).
[71] Y. In *et al*., Nucl. Fusion **59**, 056009 (2019).

[72] G. T. A. Huysmans, S. Pamela, E. van der Plas, and P. Ramet, Plasma Phys. Control. Fusion **51**, 124012 (2009).
[73] M. Hoelzl *et al*., Nucl. Fusion **61**, 065001 (2021).
[74] F. Orain *et al*., Phys. Plasmas **20**, 102510 (2013).
[75] F. Orain *et al*., Phys. Plasmas **26**, 042503 (2019).
[76] S. K. Kim *et al.*, Nucl. Fusion **60**, 026009 (2020).
[77] M. Becoulet *et al.*, Phys. Rev. Lett. **113**, 115001 (2014).
[78] J. Kim, S. S. Kim and Hogun Jhang, Nucl. Fusion **59**, 096019 (2019).
[79] A. H. Boozer, Phys. Rev. Lett. **86**, 5059 (2001).
[80] J. T. Scoville *et al.*, Nucl. Fusion **31**, 875 (1991).
[81] Y. In, J.-K. Park, Y. M. Jeon, J. Kim and M. Okabayashi, Nucl. Fusion **55**, 043004 (2015).
[82] S. M. Yang *et al*., Nucl. Fusion **61**, 086009 (2021).
[83] M. J. Lanctot, *et al.*, Phys. Plasmas **24**, 056117 (2017).
[84] K. C. Shaing, Phys. Fluids **26**, 3315 (1986).
[85] J.-K. Park *et al*., Phys. Rev. Lett. **126**, 125001 (2021).
[86] C. Nührenberg and R. Zille, Phys. Lett. **129A**, 113 (1988).
[87] A. H. Boozer, Plasma Phys. Control. Fusion **37**, A103 (1995).
[88] K. Kim *et al.*, Nucl. Fusion **57**, 036014 (2017).
[89] K. Kim *et al.*, Nucl. Fusion **57**, 126035 (2017).
[90] A. Bortolon *et al.*, Phys. Rev. Lett. **110**, 265008 (2013).
[91] M. Garcia-Munoz *et al*., Plasma Phys. Control. Fusion **61**, 054007 (2019).
[92] K. Kim, H. Jhang, J. Kim, and T. Rhee, Phys. Plasmas **25**, 122511 (2018).
[93] K. Kim, J. S. Kang, H. S. Kim and J. Kim, Nucl. Fusion **60**, 126012 (2020).
[94] K. C. Shaing, Phys. Plasmas **10**, 1443 (2003).
[95] A. M. Garofalo *et al.*, Phys. Rev. Lett. **101**, 195005 (2008).
[96] S. M. Yang *et al*., Phys. Rev. Lett. **123**, 095001 (2019).
[97] Y. Liu, M. S. Chu, I. T. Chapman, and T. C. Hender, Phys. Plasmas **15**, 112503 (2008).
[98] Z. R. Wang, M. J. Lanctot, Y. Q. Liu, J.-K. Park, and J. E. Menard, Phys. Rev. Lett. **114**, 145005 (2015).
[99] J. Kim *et al*, Rev. Sci. Instrum. **83**, 10D305 (2012).
[100] M. Garcia-Munoz *et al.*, Plasma Phys. Control. Fusion **55**, 124014 (2013).
[101] M. A. Van Zeeland *et al*., Nucl. Fusion **55**, 073028 (2015).
[102] K. G. McClements *et al*., Plasma Phys. Controlled Fusion **60**, 095005 (2018).
[103] Z. Jin *et al.*, Fusion Eng. Des. **125**, 160 (2017).
[104] J. Kim *et al*., in *15th IAEA Technical Meeting on Energetic Particles in Magnetic Confinement System* (Princeton, USA, Sept. 2017).
[105] J. Y. Kim *et al*., AIP Advances **6**, 105013 (2016).
[106] T. Rhee *et al.*, Phys. Plasmas **26**, 112504 (2019).
[107] H. P. Furth, J. Killeen, and M. N. Rosenbluth, Phys. Fluids **6**, 459 (1963).
[108] R. Fitzpatrick, Phys. Plasmas **2**, 825 (1995).
[109] K. Ida *et al.*, Phys. Plasmas **11**, 2551 (2004).
[110] E. Joffrin *et al.*, Nucl. Fusion **43**, 1167 (2003).
[111] M. J. Choi, to be submitted to RMPP (2021).
[112] M. J. Choi *et al.*, Nat. Commun. **12**, 375 (2021).
[113] G. S. Yun *et al.*, Rev. Sci. Instrum. **85**, 11D820 (2014).

[114] T. S. Hahm and P. H. Diamond, J. Korean Phys. Soc. **73**, 747 (2018).
[115] M. J. Choi *et al.*, Nucl. Fusion **56**, 066013 (2016).
[116] S. K. Kim, private communications (2021).
[117] ITER Technical Report No. ITR-20-008, 22 September 2020.
[118] G. Mckee *et al.*, Nucl. Fusion **53**, 113011 (2013).
[119] N. C. Logan, C. Zhu, J.-K. Park, S. M. Yang and Q. Hu, Nucl. Fusion **61**, 076010 (2021).

Figure Captions.

Fig. 1. (a) KSTAR three-row (Top/Middle/Bottom) in-vessel control coils and 3D fields. The coil current (in the standard 90^0 n=1 configuration) and 3D field distributions are represented in colors (reproduced from [17]). (b) Representative examples of the different n=1 coil phasings which can be applied by IVCC system in KSTAR. ϕ denotes the toroidal angle, each rectangle corresponds to one specific RMP coil with two turns, and each row represents top/middle/bottom array of the RMP coils. The plus (+) and minus (–) signs indicate the directions of the magnetic field generated by the coil currents are radially outward and inward, respectively.

Fig. 2. Impact of different RMP current strengths (I_{RMP}) on the width of q_{95} window of n=1 RMP-driven ELM-crash suppression near q_{95}~5. Shown are the time traces of q_{95}, D_α (lowest-energy spectral line of deuterium Balmer series) signal at divertor, and RMP coil current (red). Shaded area indicates the ELM-crash suppression period and arrow symbols (blue) measure the width of q_{95} window.

Fig. 3. Pedestal parameters at the T_e pedestal top position in ELMy phase before RMP (square), ELM-crash mitigation (circle) and suppression (pentagram) phases. (a) Electron temperature vs electron density, and (b) toroidal plasma rotation vs normalized electron collisionality parameter space. In (a), black dash line is ν_e* contour and green one is electron pressure contour.

Fig. 4. β_N during the ELM-crash suppression. (a) β_N vs. the neutral beam injection power (P_{NBI}). (b) β_N vs. RMP coil current (I_{RMP}).

Fig. 5. Comparison of Top/Middle vs. Bottom/Middle RMP configurations with the essentially same operational conditions. Shown in both (a) and (b) are the time evolutions of (i) RMP current amplitude per turn, (ii) toroidal phase, (iii) phase difference between rows, and (iv) photodiode signal of D_α.

Fig. 6. (a) Filamentary structure in the ELM suppression phase. (b) The cross-phase and cross-coherence measurement using ECEI channels during the ELM suppression phase.

Fig. 7. (a) Time history of integrated spectral powers of ELM and turbulence along with the RMP coil current. (b) Auto-bispectrum of a single ECEI channel in the ELM suppression phase.

Fig. 8. Time trace of perpendicular plasma flow near the pedestal with slowly increasing and decreasing RMP field strength respectively (above). Contours of 'normalized' $\boldsymbol{v}_\perp$ versus time and $\boldsymbol{\psi}_\mathbf{N}$ in the transition into and out of ELM suppression (reproduced from [57]).

Fig. 9. (a) Time trace of EHO measured by beam emission spectroscopy (BES) and Mirnov coil array. (b) Cross-bispectrum using two BES signals.

Fig. 10. Comparison of resonant field profiles of edge localized RMP and edge and core dominant RMP for KSTAR ELM suppression target discharge #18730.

Fig. 11. The time traces of main plasma parameters of KSTAR H-mode discharge with 90° phasing (#26014) and edge localized RMP (#26015). (a) Plasma currents (I_P), (b) top RMP coil current (I_T), (c) poloidal $\mathbf{D}_{\boldsymbol{\alpha}}$, (d) normalized beta ($\beta_N$).

Fig. 12. (Left) The stability diagram predicting resonant locking (red), ELM suppression (blue), non-resonant response (green) as a function of mid-coil n=1 current and phasing, with a fixed top and bottom coil currents. (A-F) orange lines show experimental 3D field traces and blue lines indicate ELM suppression validated in experiments. (Right) D-alpha measurements showing ELM suppression windows for each (A-F) traces as indicated as blue windows as well. Note in (A-C) ELM suppression was found while decreasing mid-coil currents as predicted in the diagram.

Fig. 13. A diagram for machine learning-based real-time ELM-crash controller installed in KSTAR PCS. The LSTM classifier receives the real-time diagnostic signals and then classifies the plasma. Based on the judgment and the preset trigger conditions, the RMP current is applied.

Fig. 14. A result for initial ELM-crash suppression by the machine learning-based real-time ELM-crash controller. The KSTAR discharge #27350(cyan color) is a H-mode reference shot and the discharge #27347(blue color) is initial ELM-crash suppression shot. In the suppression shot, the RMP is applied right after receiving real-time classification result from the LSTM classifier.

Fig. 15. TM1 simulated q_{95} windows of ELM suppression by (a) n = 1 for discharge 18730 and (b) n = 2 RMP for discharge 18594 in KSTAR represented by the contour plot of simulated relative reduction of pedestal pressure versus RMP coil current I_{RMP} and q_{95}. The blue curves in (a) and (b) indicate the expected ELM suppression boundary with 15% reduction in the pedestal pressure. The experimentally observed q_{95} windows are also overlaid by black circles, and the error bar indicates the variation of q_{95} and RMP coil current during complete ELM suppression.

Fig. 16. The time evolution of n=4-14 potential perturbations of ELM harmonics is shown (left). Net mode amplitude of ELMy case (red dotted line) is suppressed by RMPs (solid lines). Filament structures (right) are observed in ELMy and the suppressed case (RMP+ELM), consistent with the experimental observation.

Fig. 17. The linear growth rate of ELMs is presented (left). Linear stability of ELM harmonics is largely decreased from ELMy (red) phase to the suppressed phase (blue) by the pedestal degradation. The time evolution of potential perturbations of ELM (right) reveals that ELMy (red) and the case with degraded pedestal by RMP (blue) still exhibits bursty behavior during their nonlinear phase. ELM suppression is achieved when the degraded pedestal and mode coupling effect are introduced simultaneously (orange).

Fig. 18. The time traces of main plasma parameters of KSTAR Ohmic discharge #16105. (a) n=1 Amplitude of IVCC coil and plasma currents (b) line-averaged plasma density, (c) electron temperature (d) toroidal mode amplitudes. The time traces of main plasma parameters of KSTAR Ohmic discharge #19111. (e) n=2 Amplitude of IVCC coil and plasma currents (f) line-averaged plasma density, (g) electron temperature (h) toroidal mode amplitudes.

Fig. 19. n=1 (circle) and n=2 (triangle) error field threshold at various density with three different resonant field criteria. (a) Overlap field (δB_{of1}), (b) 2/1 (n=1), 3/2 (n=2) IPEC resonant field (δB_{21}), and (c) 2/1 (n=1), 3/2 (n=2) vacuum resonant field (δB_{21}^{vac}) in KSTAR Ohmic discharges with $\mathbf{B_T}$= 2T, $\mathbf{I_p}$= 0.6MA.

Fig. 20. Impact of QSMP, NRMP, and RMP shown by the time traces in a single KSTAR discharge; (a) 3D coil configurations with 3 n=1 amplitudes and phases (rad) for top, middle, bottom rows of in-vessel coil, (b) line-averaged electron density and electron temperature measured at R~1.98m, and (c) toroidal rotation measured at R~2.07m. (d) shows the comparison of the total integrated torque between predictions and measurements.

Fig. 21. Time traces of improved confinement discharge by magnetic braking (#22705). (b) Spectrogram from the Mirnov coils showing the TAE mode activities (indicated in the figure) in the magnetic braking discharge (#22698).

Fig. 22. The time traces of main plasma parameters in KSTAR discharges. (a) Amplitude of IVCC coil currents (I_{IVCC}), (b) line-averaged plasma density ($\overline{n_e}$), (c) core electron (T_e) and ion (T_i) temperature, and (d) toroidal rotation frequency measured at the center ($\omega_{\phi 0}$) and at the q~2 [ω_ϕ (q~2)] location. Figure is reproduced from [92].

Fig. 23. (a) Radial profiles of toroidal rotation frequency for #19115 at t = 2.35 s and t = 2.55 s, with electron and ion offset rate at t =2.55 s. (b) Comparison of measured (red, square) and calculated NTV torque with (blue, solid) and without (black, dashed) resistive response in MARS-K simulations.

Fig. 24. (a) IVCC current oscillation of middle P port, and (b) temperature increase of poloidal limiter 3 (red). Black line in (b) is temperature increase without RMP field with same plasma situation but different shot. Applying RMP field increases poloidal limiter temperature.

Fig. 25. (a) Fast ion loss signal measured by FILD probe and (b) simulation result of toroidally rotating 3D field.

Fig. 26. (a) Change of the electron temperature fluctuation power before and after the magnetic island whose boundary is indicated by purple dashed lines. (b) Fluctuation phase velocity in the laboratory frame around the island. Figure is reproduced from [32].

Fig. 27. (a) Turbulence spreading from the outside (inner region; $r < r_{si}$ where r_{si} is the inner separatrix of the island) of the island into the inside of the island. It carries the heat flux leading to the temperature peaking inside the island. (b) Change of electron temperature and the normalized fluctuation amplitude near the X-point of the island. Figure is reproduced from [108].

Fig. 28. Energy flow from the plasma to the SOL and outer divertor target.

Fig. 29. An example of the heat flux profile onto the outer divertor target predicted by EMC3-EIRENE (1) without and (2) with MPs.

Fig. 30. The measurement of the divertor heat flux profile according to the different configuration of MPs.

Fig. 31. The comparison of the divertor heat flux profiles with/without MPs.

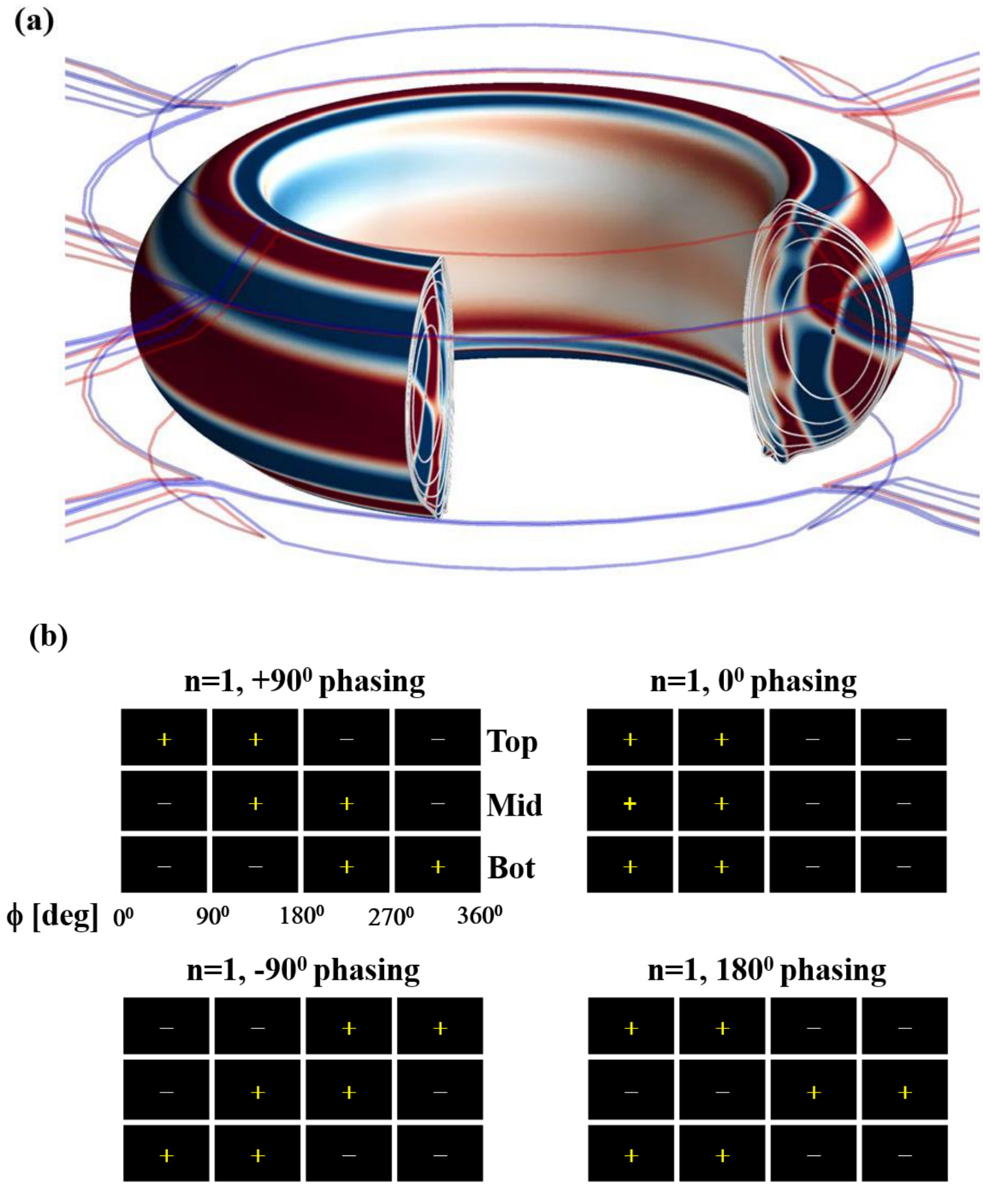
(a)
(b)
n=1, +90⁰ phasing
n=1, 0⁰ phasing
Top
Mid
Bot
ϕ [deg] 0⁰ 90⁰ 180⁰ 270⁰ 360⁰
n=1, -90⁰ phasing
n=1, 180⁰ phasing

Fig. 1.

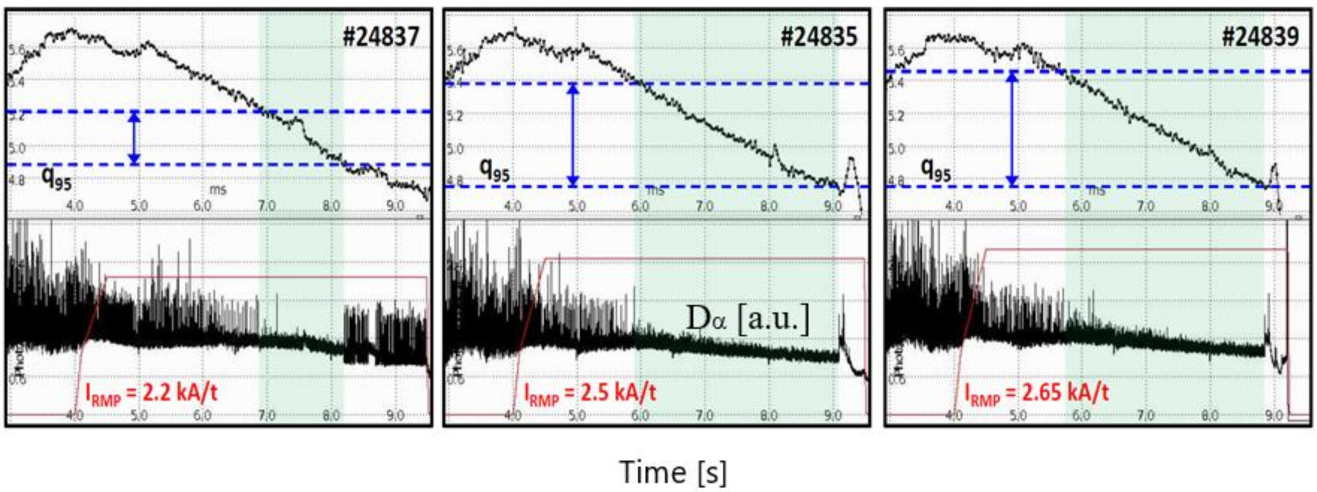
#24837
#24835
#24839
q_{95}
I_{RMP} = 2.2 kA/t
I_{RMP} = 2.5 kA/t
I_{RMP} = 2.65 kA/t
Dα [a.u.]
Time [s]

Fig. 2.

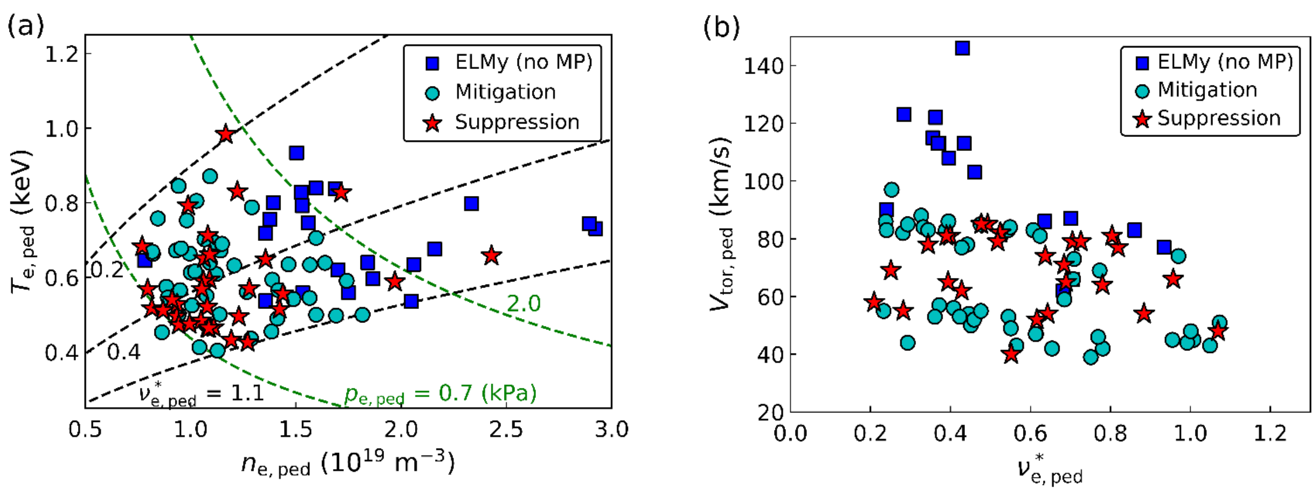
(a)
ELMy (no MP)
Mitigation
Suppression
$T_{\mathrm{e,ped}}$ (keV)
$n_{\mathrm{e,ped}}$ (10^{19} m^{-3})
0.2
0.4
$\nu^*_{\mathrm{e,ped}}$ = 1.1
2.0
$p_{\mathrm{e,ped}}$ = 0.7 (kPa)
(b)
ELMy (no MP)
Mitigation
Suppression
$V_{\mathrm{tor,ped}}$ (km/s)
$\nu^*_{\mathrm{e,ped}}$

Fig. 3.

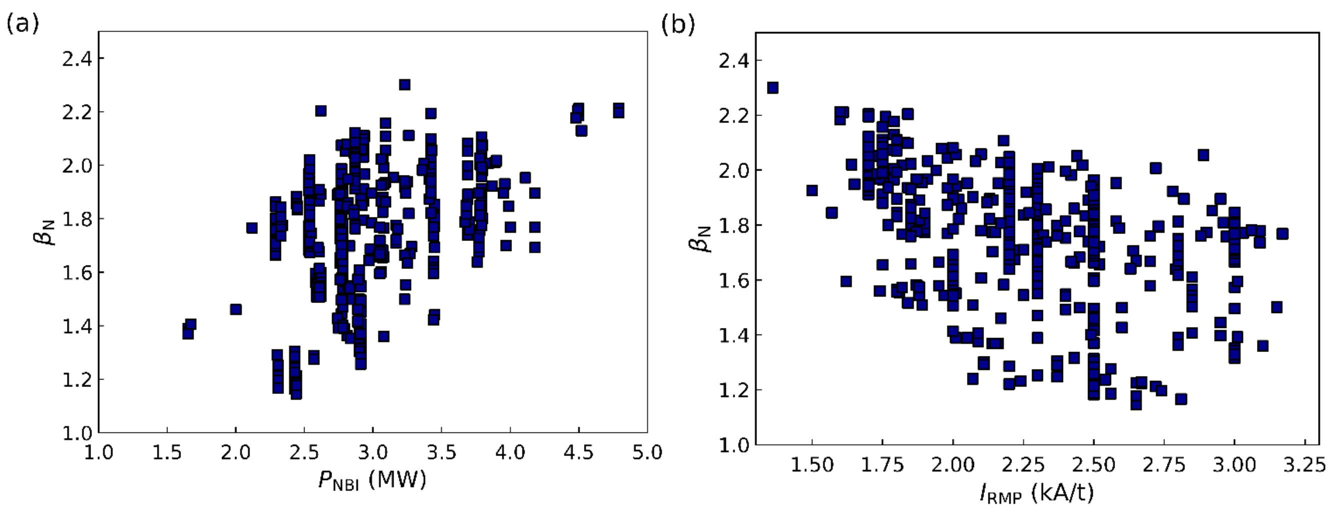
(a)
2.4
2.2
2.0
1.8
1.6
1.4
1.2
1.0
β_N
1.0 1.5 2.0 2.5 3.0 3.5 4.0 4.5 5.0
P_{NBI} (MW)
(b)
2.4
2.2
2.0
1.8
1.6
1.4
1.2
1.0
β_N
1.50 1.75 2.00 2.25 2.50 2.75 3.00 3.25
I_{RMP} (kA/t)

Fig. 4.

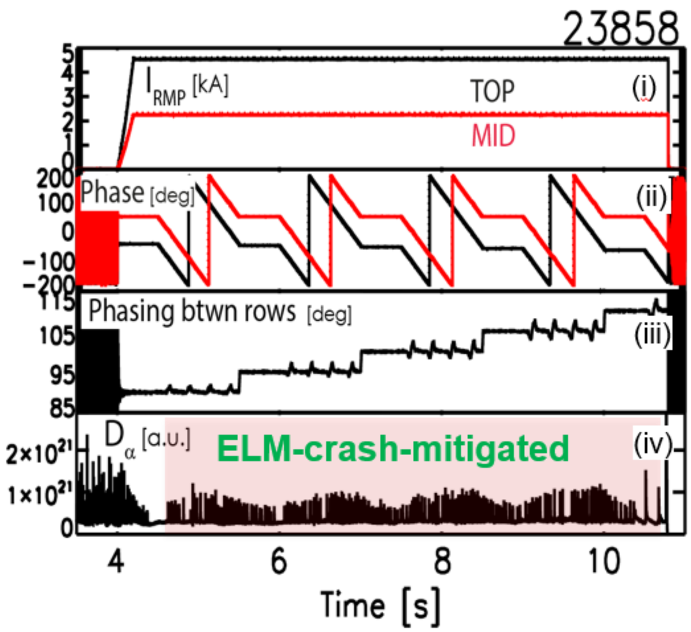
23858
I_{RMP} [kA]
TOP
MID
(i)
Phase [deg]
(ii)
Phasing btwn rows [deg]
(iii)
D_α [a.u.]
ELM-crash-mitigated
(iv)
Time [s]

(a)

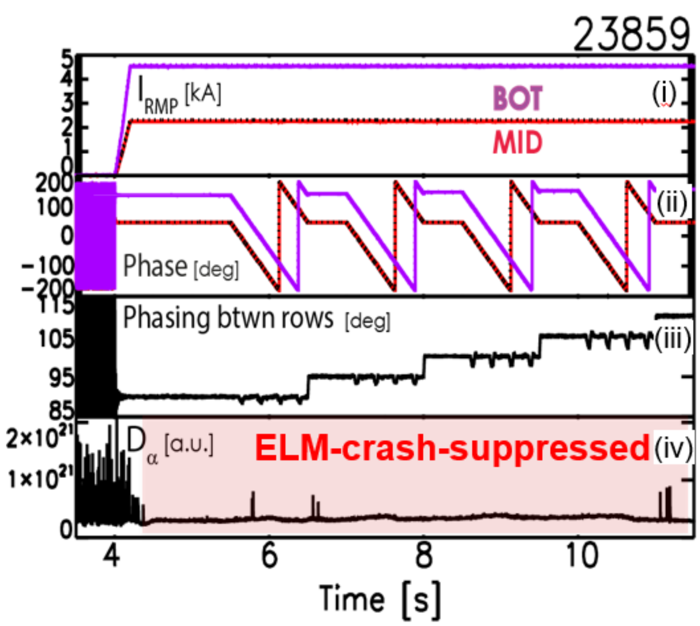
23859
I_{RMP} [kA]
BOT
MID
(i)
Phase [deg]
(ii)
Phasing btwn rows [deg]
(iii)
D_α [a.u.]
ELM-crash-suppressed
(iv)
Time [s]

(b)

Fig. 5.

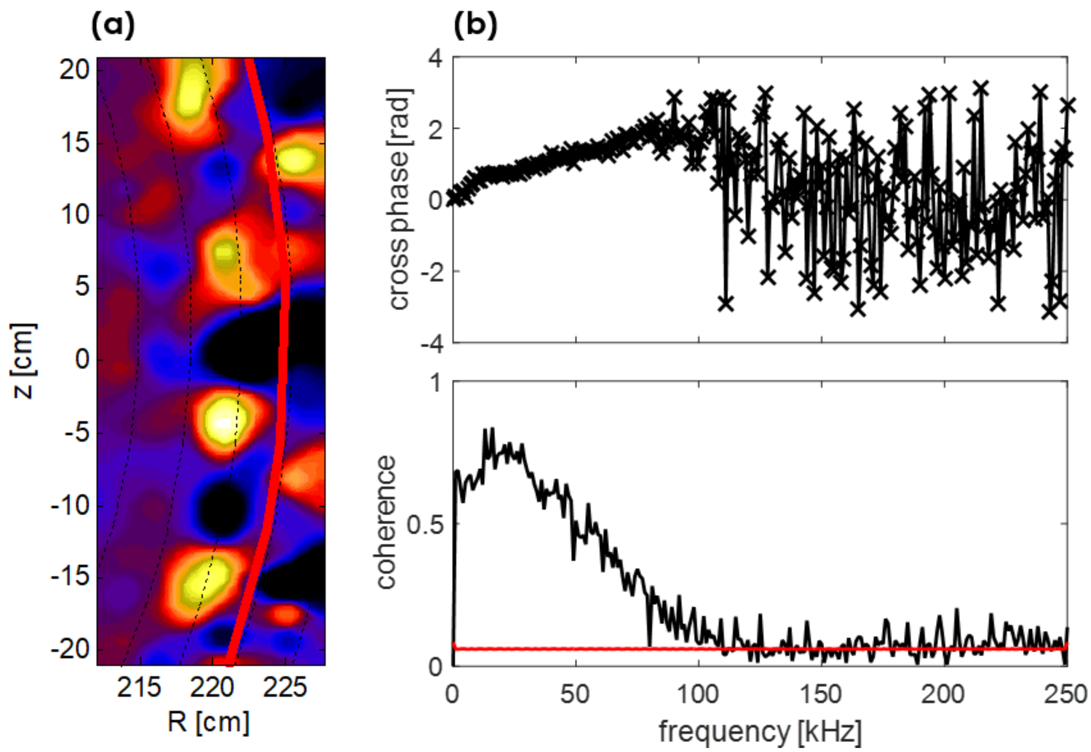

(a)
(b)
20
15
10
5
0
-5
-10
-15
-20
z [cm]
215
220
225
R [cm]
4
2
0
-2
-4
cross phase [rad]
1
0.5
0
coherence
0
50
100
150
200
250
frequency [kHz]

Fig. 6.

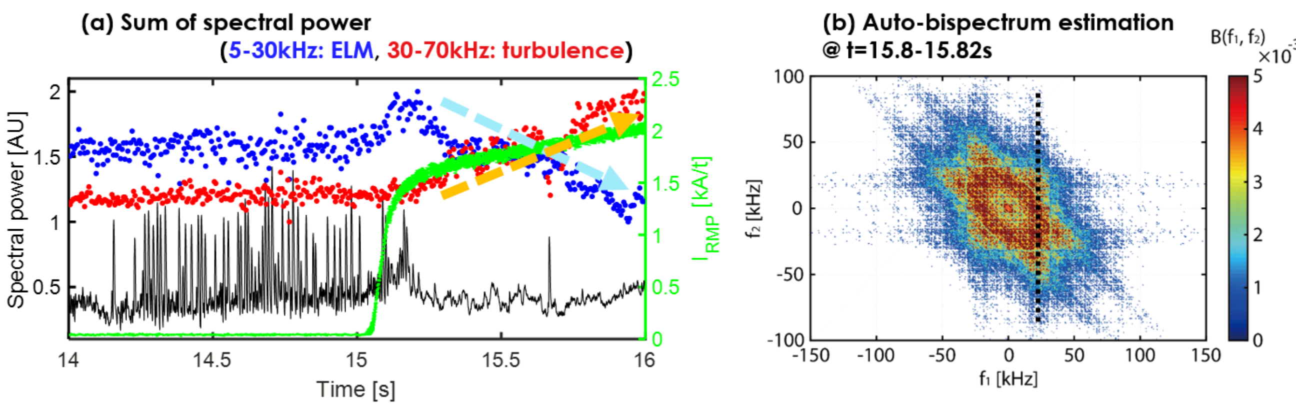
(a) Sum of spectral power
(5-30kHz: ELM, 30-70kHz: turbulence)
Spectral power [AU]
I_{RMP} [kA/t]
Time [s]
14
14.5
15
15.5
16
(b) Auto-bispectrum estimation
@ t=15.8-15.82s
B(f₁, f₂)
×10⁻³
f₂ [kHz]
f₁ [kHz]

Fig. 7.

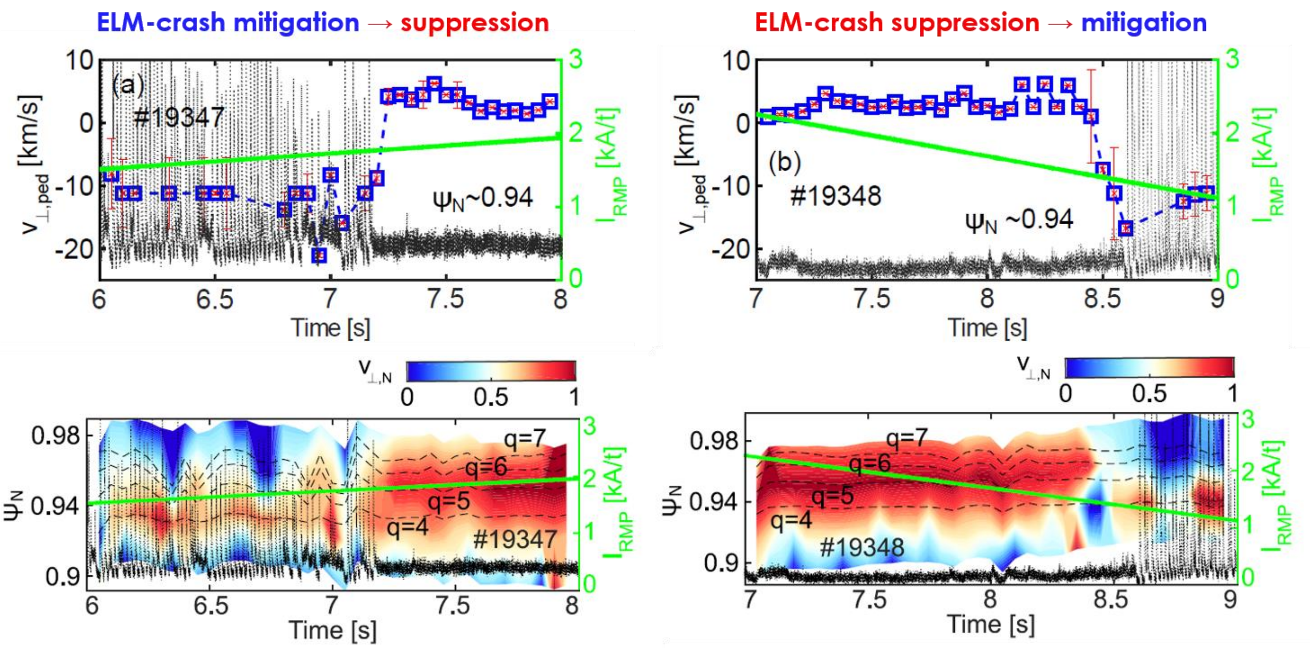

ELM-crash mitigation → suppression
ELM-crash suppression → mitigation
(a)
#19347
ψN~0.94
(b)
#19348
ψN ~0.94
v⊥,ped [km/s]
IRMP [kA/t]
Time [s]
v⊥,N
ψN
q=7
q=6
q=5
q=4
#19347
#19348

Fig. 8.

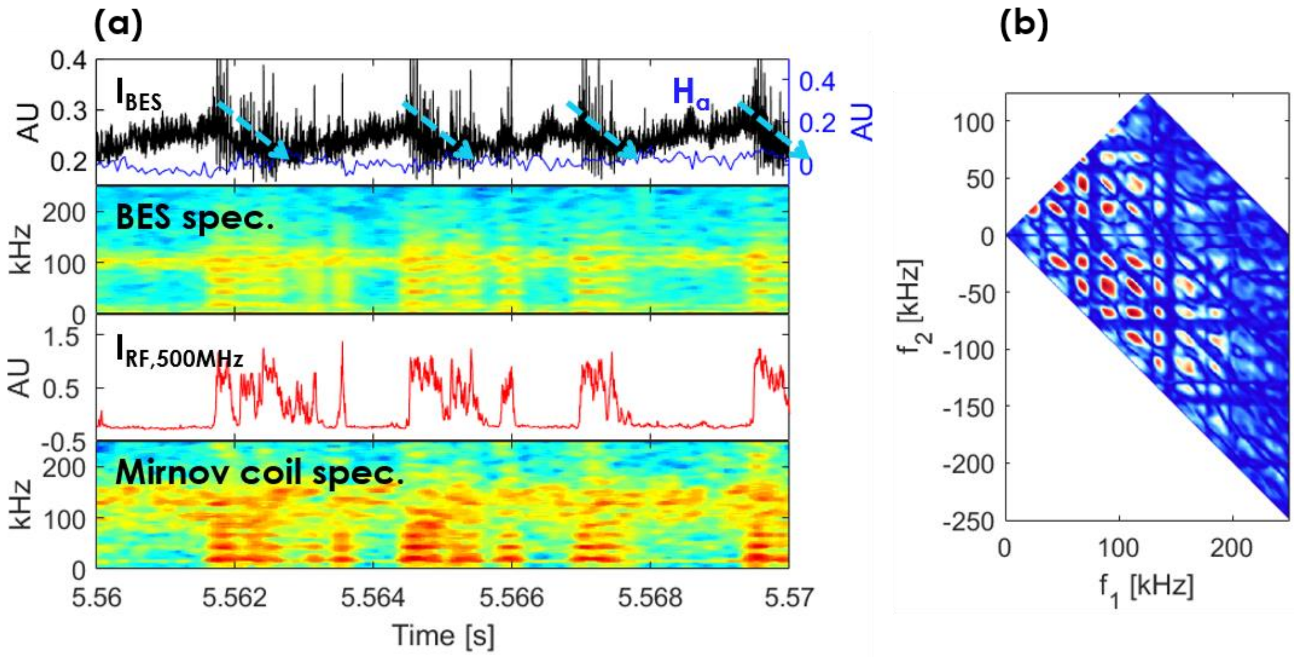
(a)
(b)
I_{BES}
H_α
AU
BES spec.
kHz
$I_{RF,500MHz}$
Mirnov coil spec.
Time [s]
f_2 [kHz]
f_1 [kHz]

Fig. 9.

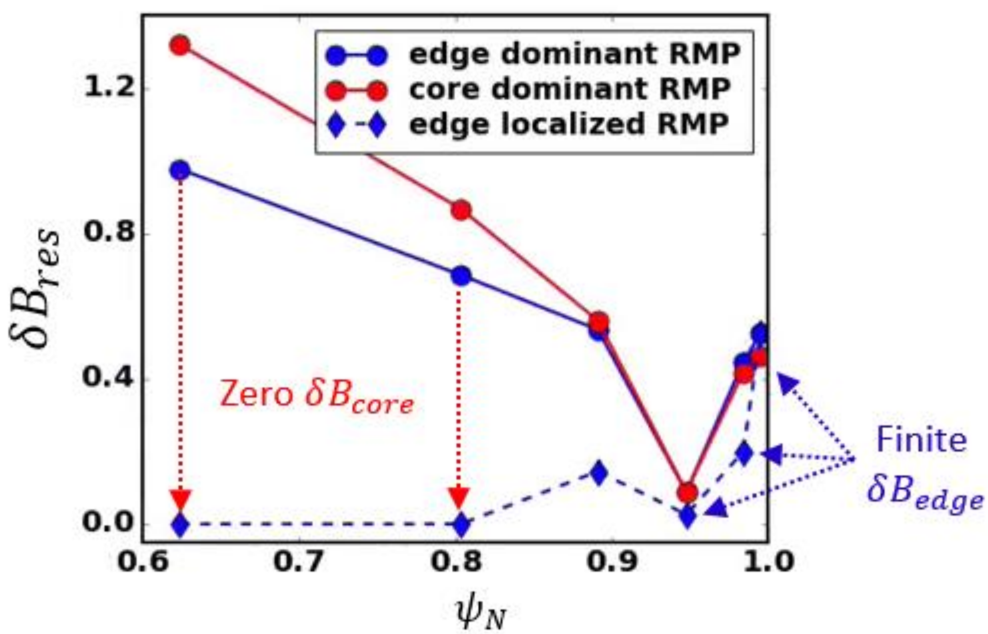
edge dominant RMP
core dominant RMP
edge localized RMP
1.2
0.8
0.4
0.0
0.6
0.7
0.8
0.9
1.0
δB_{res}
ψ_N
Zero δB_{core}
Finite
δB_{edge}

Fig. 10.

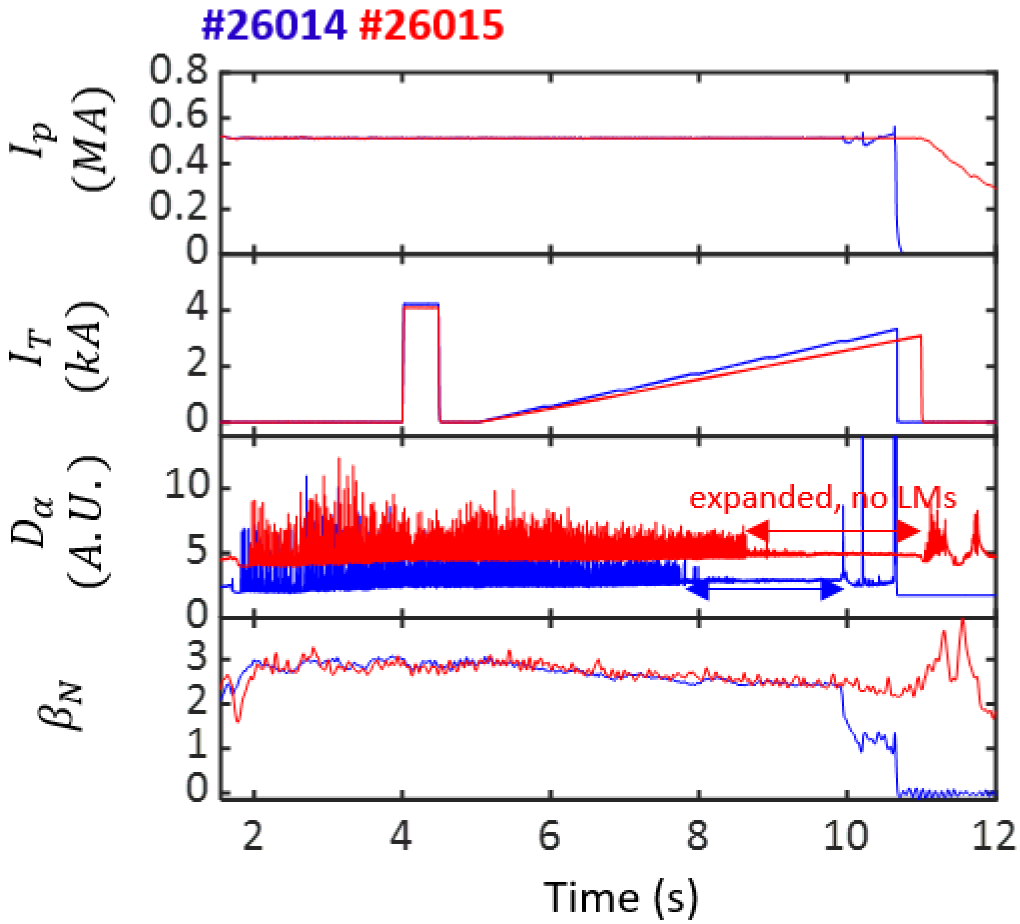

Fig. 11.

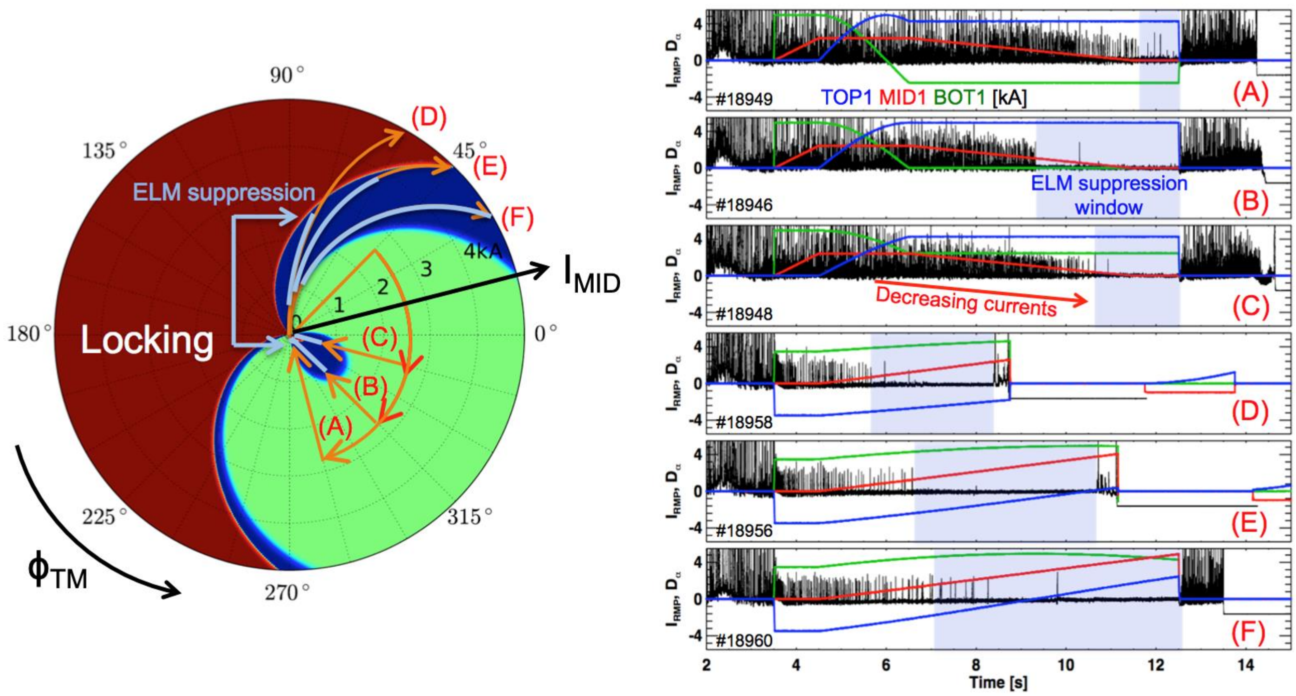
90°
135°
45°
180°
0°
225°
315°
270°
(D)
(E)
(F)
(C)
(B)
(A)
ELM suppression
Locking
1
2
3
4kA
I_{MID}
ϕ_{TM}
#18949
TOP1 MID1 BOT1 [kA]
#18946
ELM suppression window
#18948
Decreasing currents
#18958
#18956
#18960
I_{RMP}, D_α
Time [s]

Fig. 12.

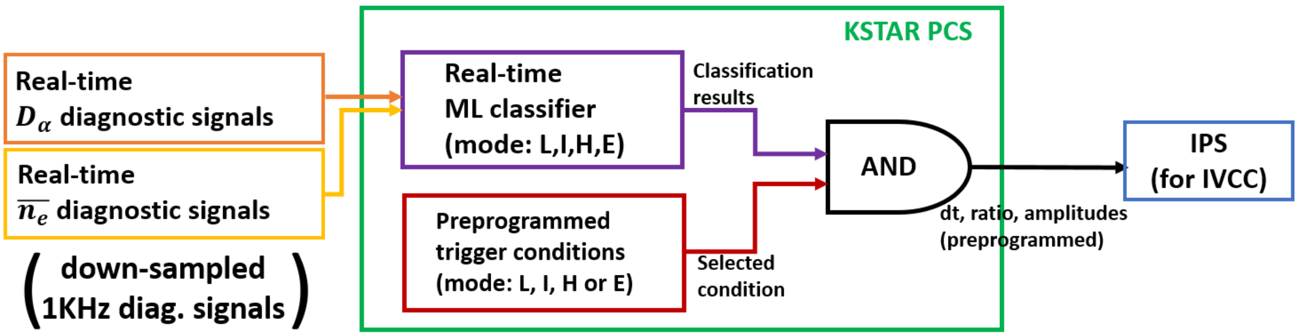
KSTAR PCS
Real-time
D_α diagnostic signals
Real-time
$\overline{n_e}$ diagnostic signals
down-sampled
1KHz diag. signals
Real-time
ML classifier
(mode: L,I,H,E)
Classification
results
Preprogrammed
trigger conditions
(mode: L, I, H or E)
Selected
condition
AND
dt, ratio, amplitudes
(preprogrammed)
IPS
(for IVCC)

Fig. 13.

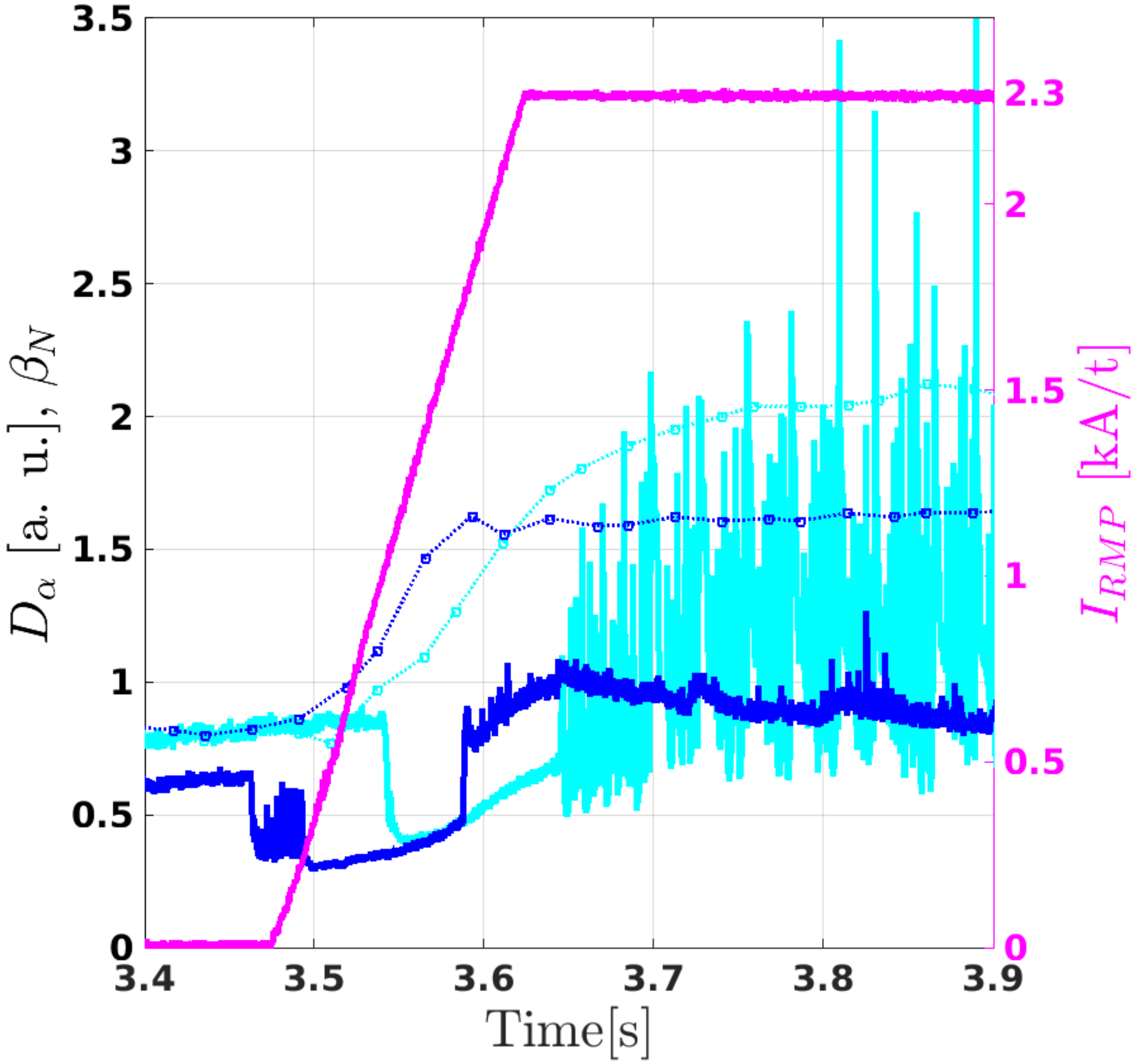

3.5
3
2.5
2
1.5
1
0.5
0
D_α [a. u.], β_N
3.4
3.5
3.6
3.7
3.8
3.9
Time[s]
2.3
2
1.5
1
0.5
0
I_{RMP} [kA/t]

Fig. 14.

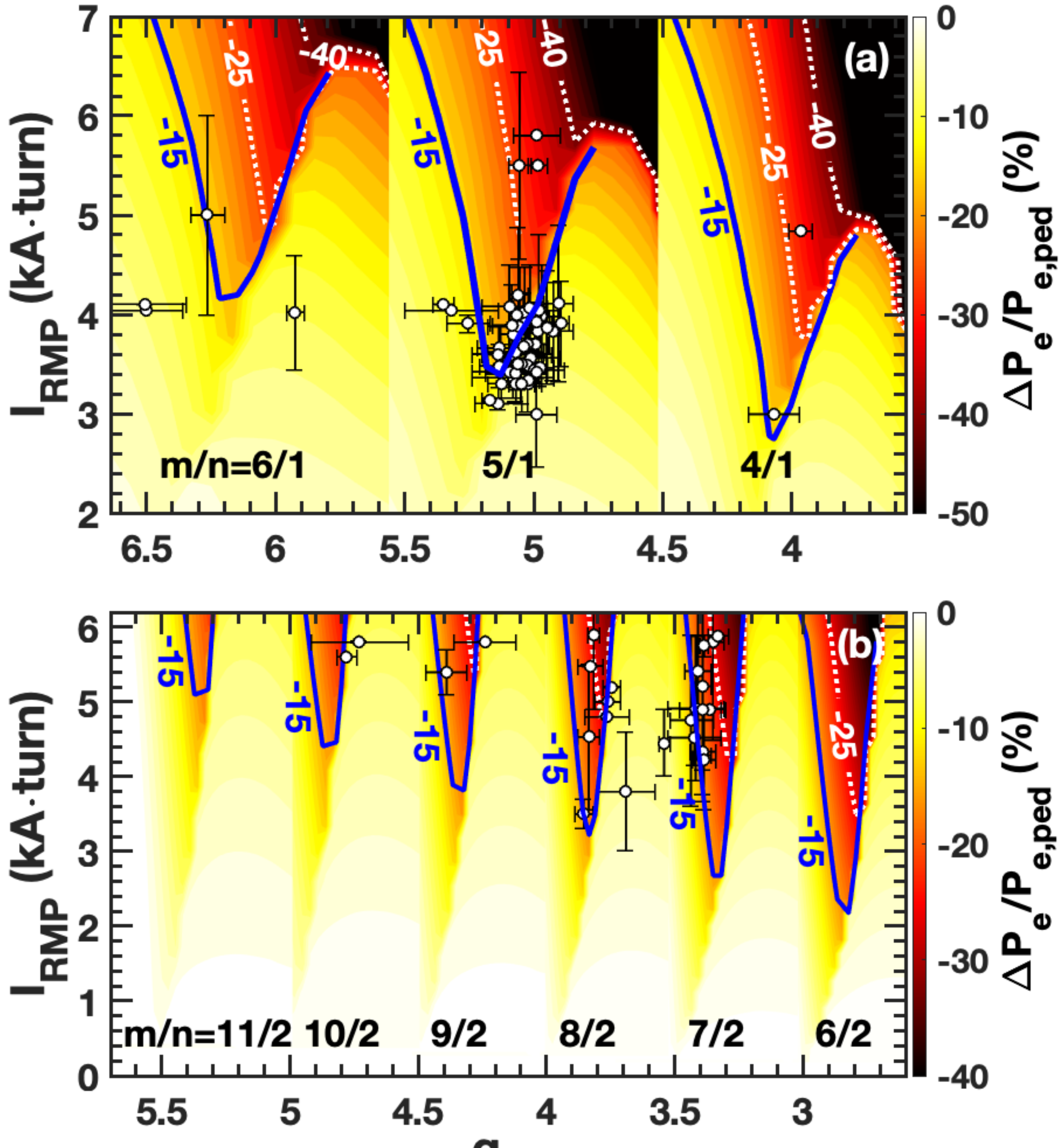

(a)
-15
-25
-40
25
m/n=6/1
5/1
4/1
I_{RMP} (kA·turn)
$\Delta P_e/P_{e,ped}$ (%)
(b)
m/n=11/2
10/2
9/2
8/2
7/2
6/2
q_{95}

Fig. 15.

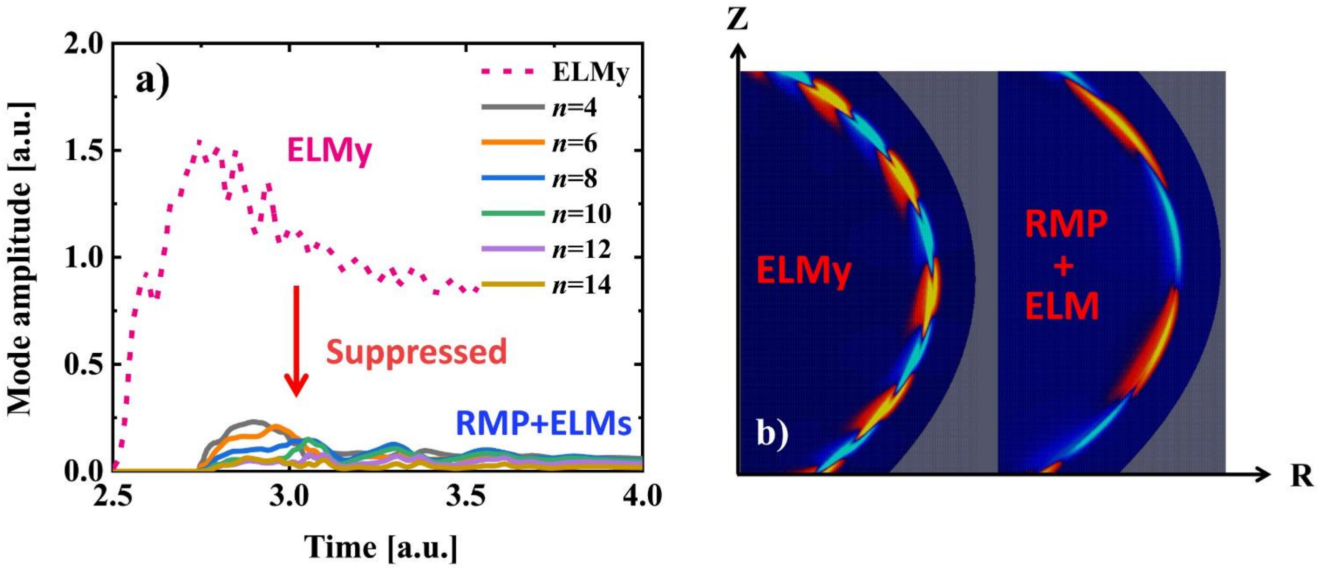
a)
2.0
1.5
1.0
0.5
0.0
2.5
3.0
3.5
4.0
Mode amplitude [a.u.]
Time [a.u.]
ELMy
n=4
n=6
n=8
n=10
n=12
n=14
ELMy
Suppressed
RMP+ELMs
Z
R
ELMy
RMP
+
ELM
b)

Fig. 16.

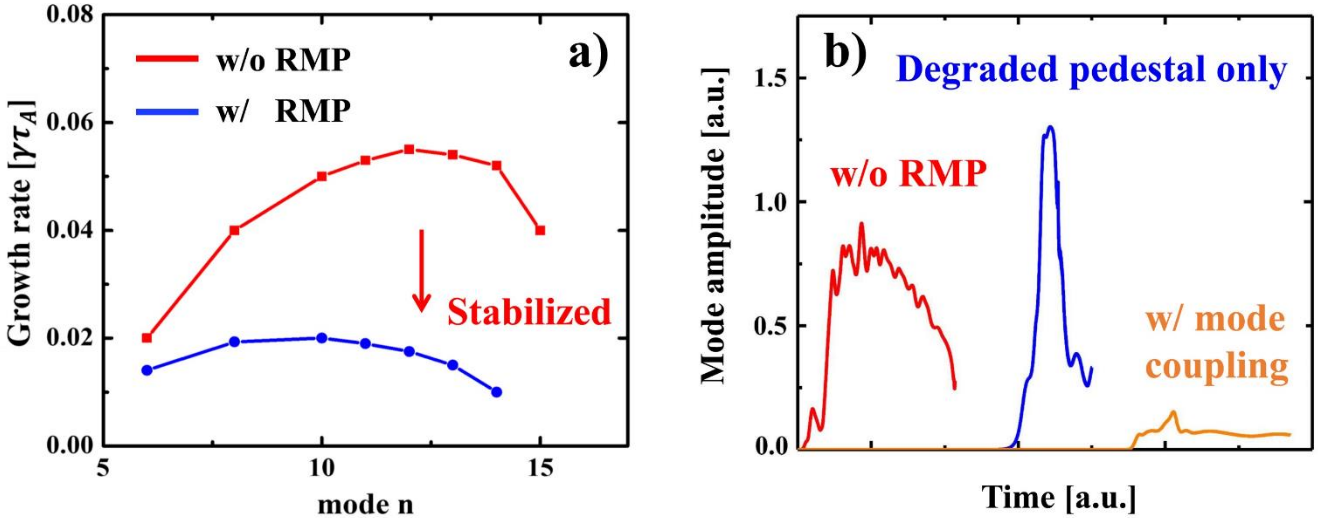

a)
w/o RMP
w/ RMP
Stabilized
Growth rate [$\gamma\tau_A$]
mode n
0.08
0.06
0.04
0.02
0.00
5
10
15
b)
Degraded pedestal only
w/o RMP
w/ mode coupling
Mode amplitude [a.u.]
Time [a.u.]
1.5
1.0
0.5
0.0

Fig. 17.

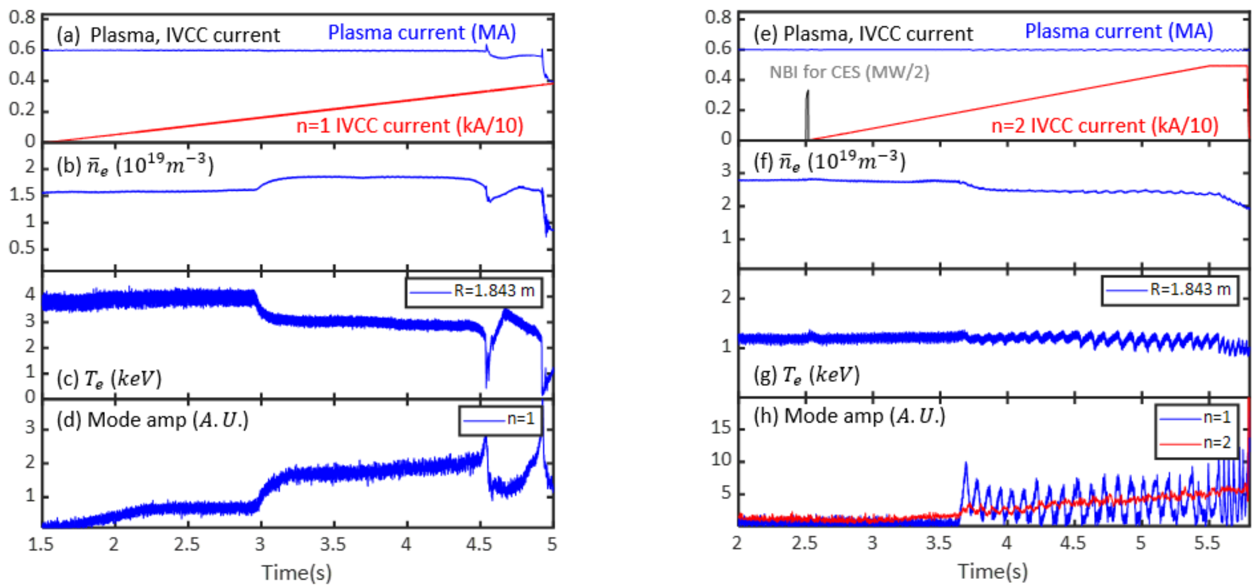

(a) Plasma, IVCC current
Plasma current (MA)
n=1 IVCC current (kA/10)
(b) $\bar{n}_e$ $(10^{19}m^{-3})$
R=1.843 m
(c) T_e (keV)
(d) Mode amp $(A.U.)$
n=1
Time(s)
(e) Plasma, IVCC current
Plasma current (MA)
NBI for CES (MW/2)
n=2 IVCC current (kA/10)
(f) $\bar{n}_e$ $(10^{19}m^{-3})$
R=1.843 m
(g) T_e (keV)
(h) Mode amp $(A.U.)$
n=1
n=2
Time(s)

Fig. 18.

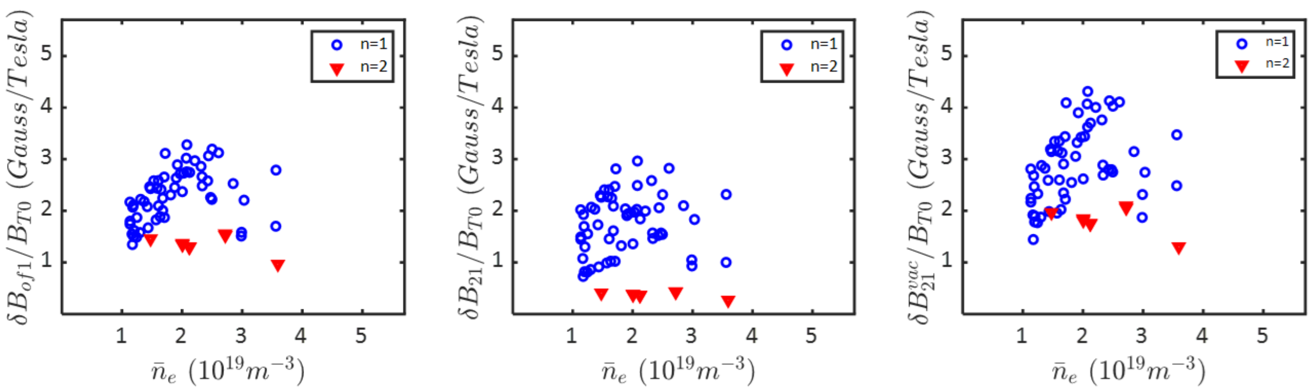

$\delta B_{of1}/B_{T0}$ $(Gauss/Tesla)$
$\bar{n}_e$ $(10^{19}m^{-3})$
n=1
n=2
$\delta B_{21}/B_{T0}$ $(Gauss/Tesla)$
$\bar{n}_e$ $(10^{19}m^{-3})$
n=1
n=2
$\delta B_{21}^{vac}/B_{T0}$ $(Gauss/Tesla)$
$\bar{n}_e$ $(10^{19}m^{-3})$
n=1
n=2

Fig. 19.

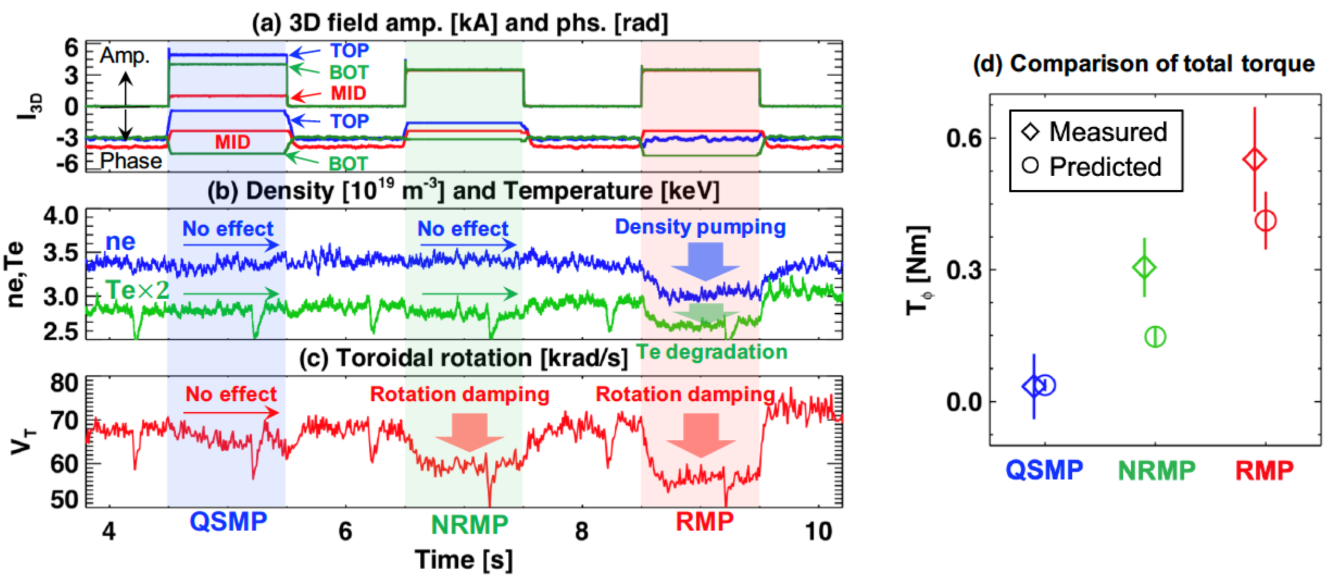

(a) 3D field amp. [kA] and phs. [rad]
I3D
Amp.
Phase
TOP
BOT
MID
TOP
MID
BOT
(b) Density [10^19 m^-3] and Temperature [keV]
ne,Te
ne
Te×2
No effect
No effect
Density pumping
Te degradation
(c) Toroidal rotation [krad/s]
VT
No effect
Rotation damping
Rotation damping
QSMP
NRMP
RMP
Time [s]
(d) Comparison of total torque
Measured
Predicted
Tϕ [Nm]
QSMP
NRMP
RMP

Fig. 20.

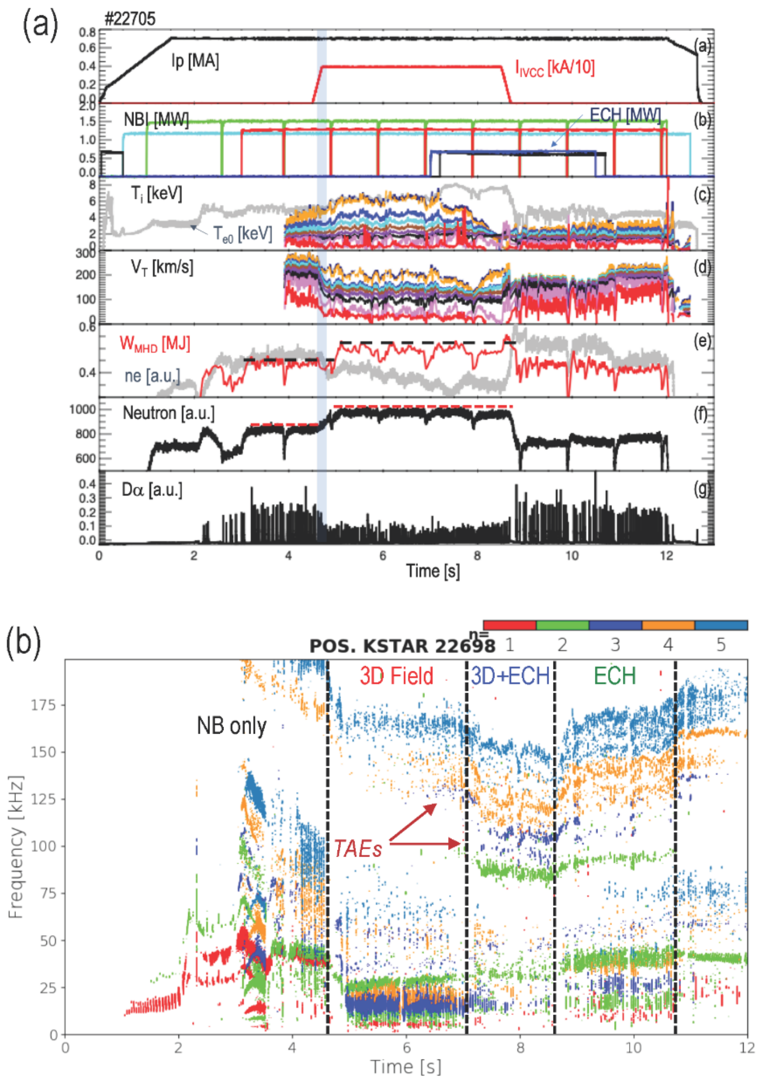

(a)
#22705
Ip [MA]
I_{IVCC} [kA/10]
NBI [MW]
ECH [MW]
T_i [keV]
T_{e0} [keV]
V_T [km/s]
W_{MHD} [MJ]
ne [a.u.]
Neutron [a.u.]
Dα [a.u.]
Time [s]
(b)
POS. KSTAR 22698
n= 1 2 3 4 5
NB only
3D Field
3D+ECH
ECH
TAEs
Frequency [kHz]
Time [s]

Fig. 21.

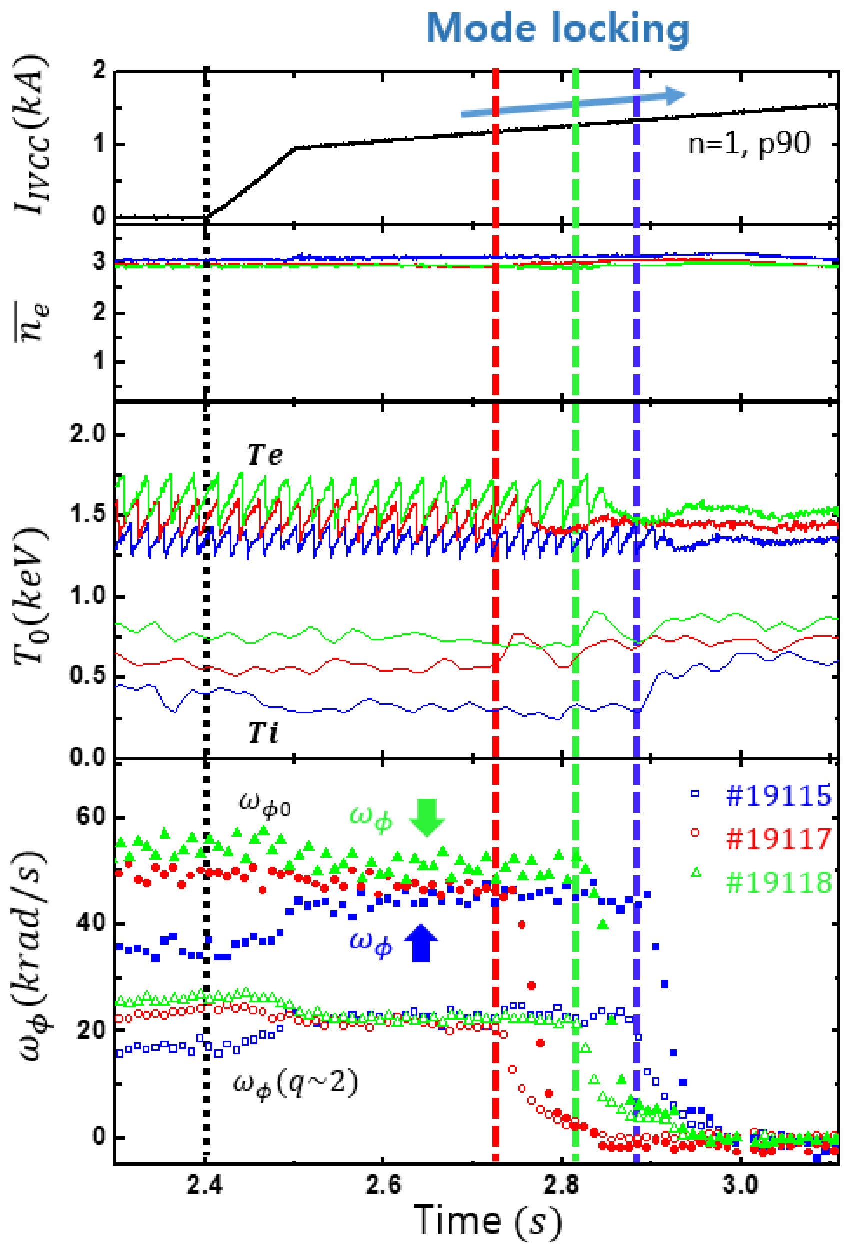
Mode locking
$I_{IVCC}(kA)$
n=1, p90
$\overline{n_e}$
Te
$T_0(keV)$
Ti
$\omega_{\phi 0}$
ω_ϕ
#19115
#19117
#19118
$\omega_\phi(krad/s)$
$\omega_\phi(q\sim2)$
Time (s)

Fig. 22.

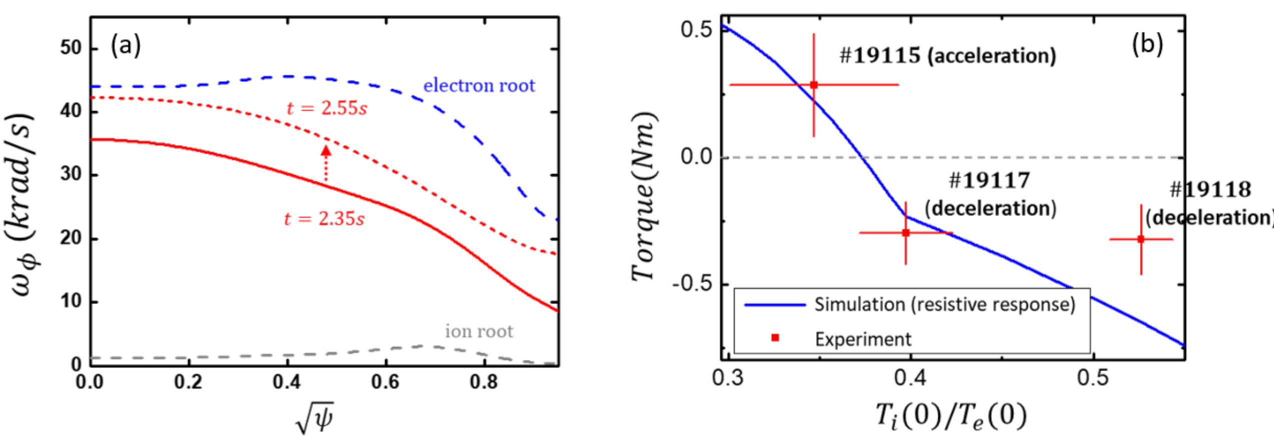

(a)
electron root
$t = 2.55s$
$t = 2.35s$
ion root
$\omega_\phi\ (krad/s)$
$\sqrt{\psi}$
(b)
#19115 (acceleration)
#19117 (deceleration)
#19118 (deceleration)
Simulation (resistive response)
Experiment
$Torque(Nm)$
$T_i(0)/T_e(0)$

Fig. 23.

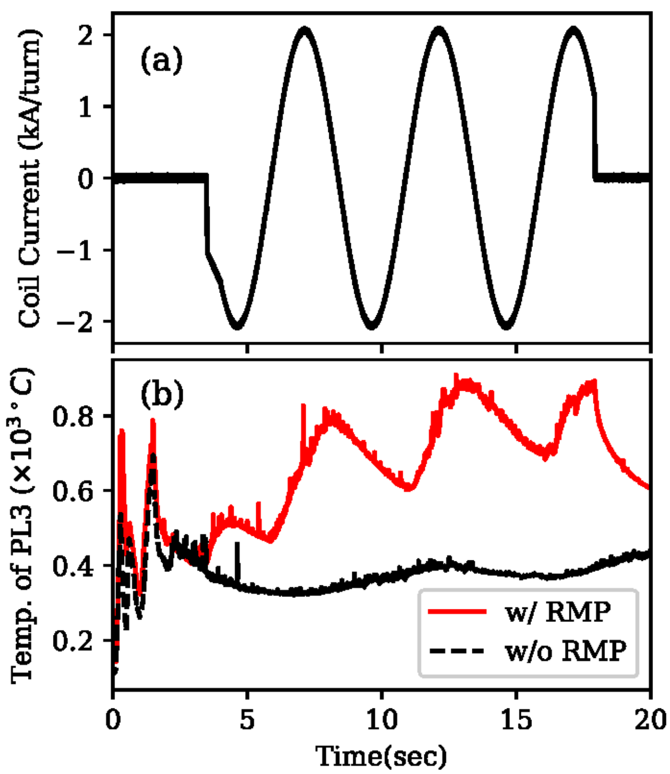

(a)
Coil Current (kA/turn)
2
1
0
−1
−2
(b)
Temp. of PL3 (×10³ °C)
0.8
0.6
0.4
0.2
w/ RMP
w/o RMP
0
5
10
15
20
Time(sec)

Fig. 24.

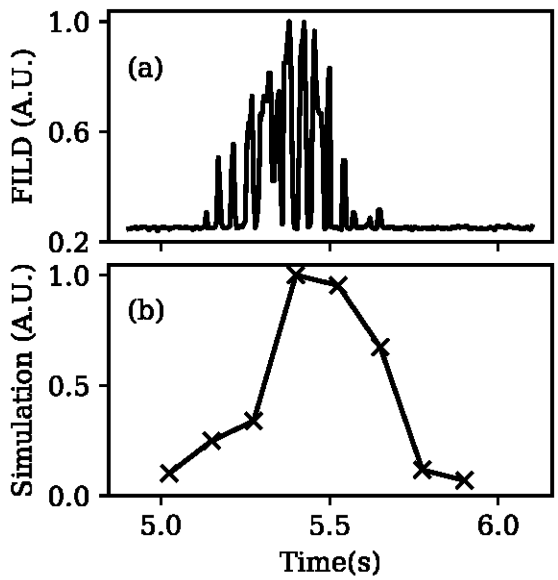

Fig. 25.

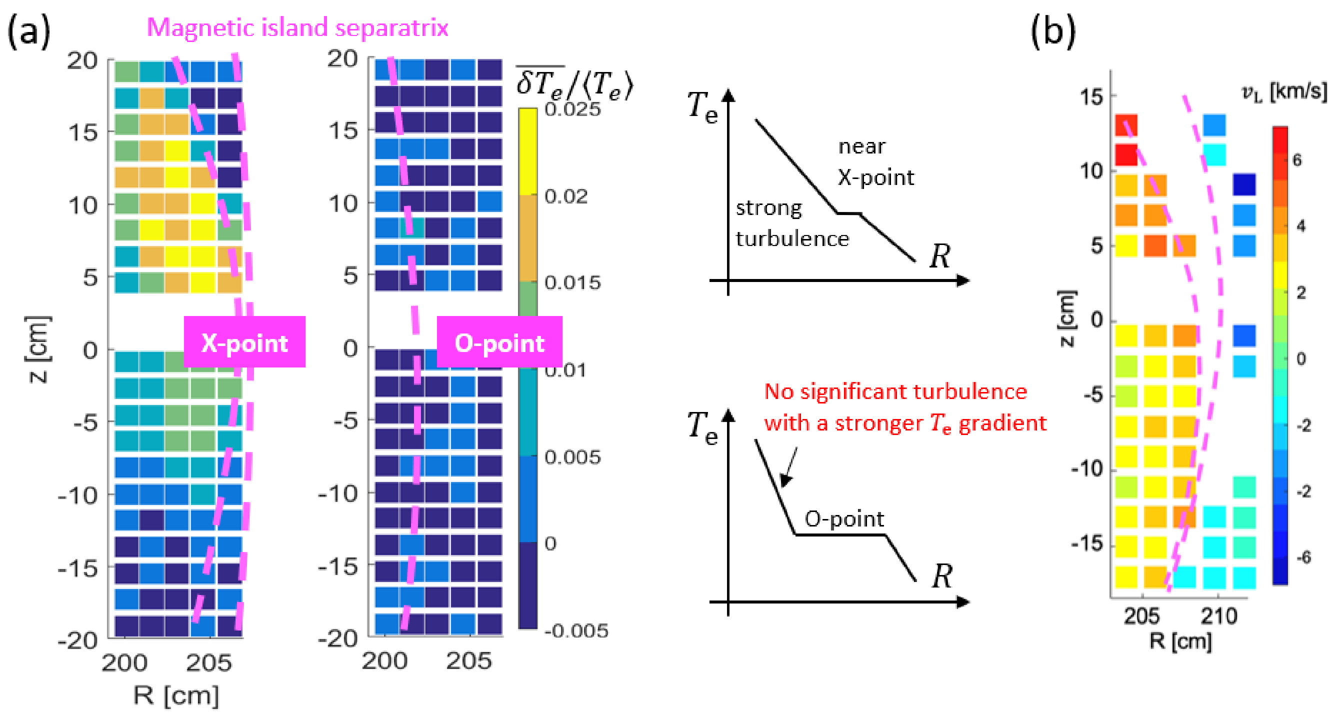

(a)
Magnetic island separatrix
X-point
O-point
$\overline{\delta T_e}/\langle T_e \rangle$
z [cm]
R [cm]
T_e
near
X-point
strong
turbulence
R
No significant turbulence
with a stronger T_e gradient
O-point
(b)
v_L [km/s]
z [cm]
R [cm]

Fig. 26.

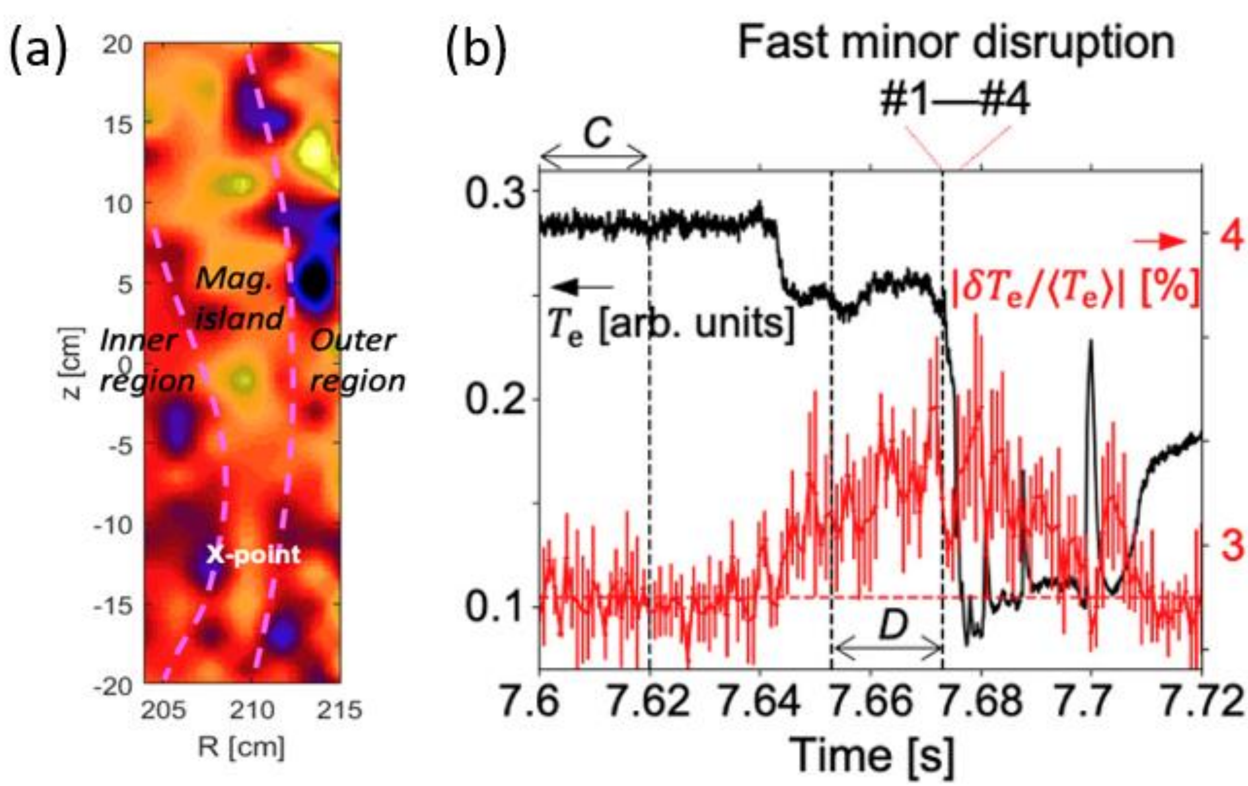

(a)
Mag. island
Inner region
Outer region
X-point
z [cm]
R [cm]
(b)
Fast minor disruption #1—#4
C
D
T_e [arb. units]
$|\delta T_e/\langle T_e\rangle|$ [%]
Time [s]

Fig. 27.

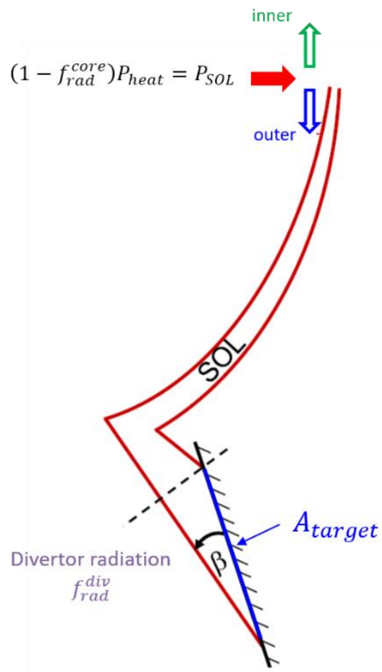
inner
$(1 - f_{rad}^{core})P_{heat} = P_{SOL}$
outer
SOL
A_{target}
β
Divertor radiation
f_{rad}^{div}

Fig. 28.

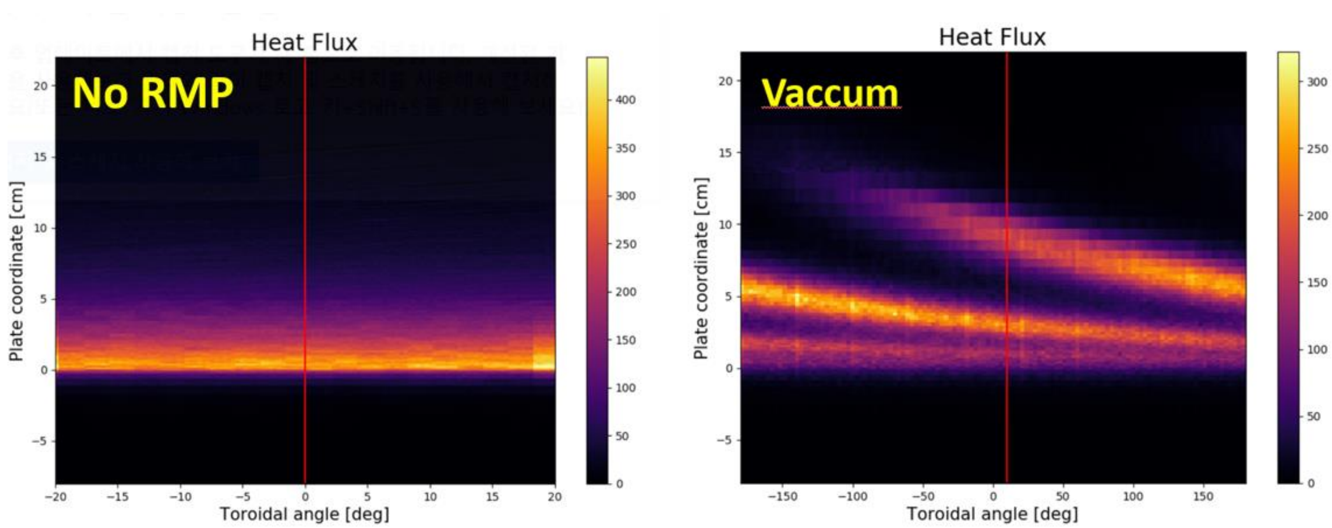
Heat Flux
No RMP
Plate coordinate [cm]
Toroidal angle [deg]
Heat Flux
Vaccum
Plate coordinate [cm]
Toroidal angle [deg]

Fig. 29.

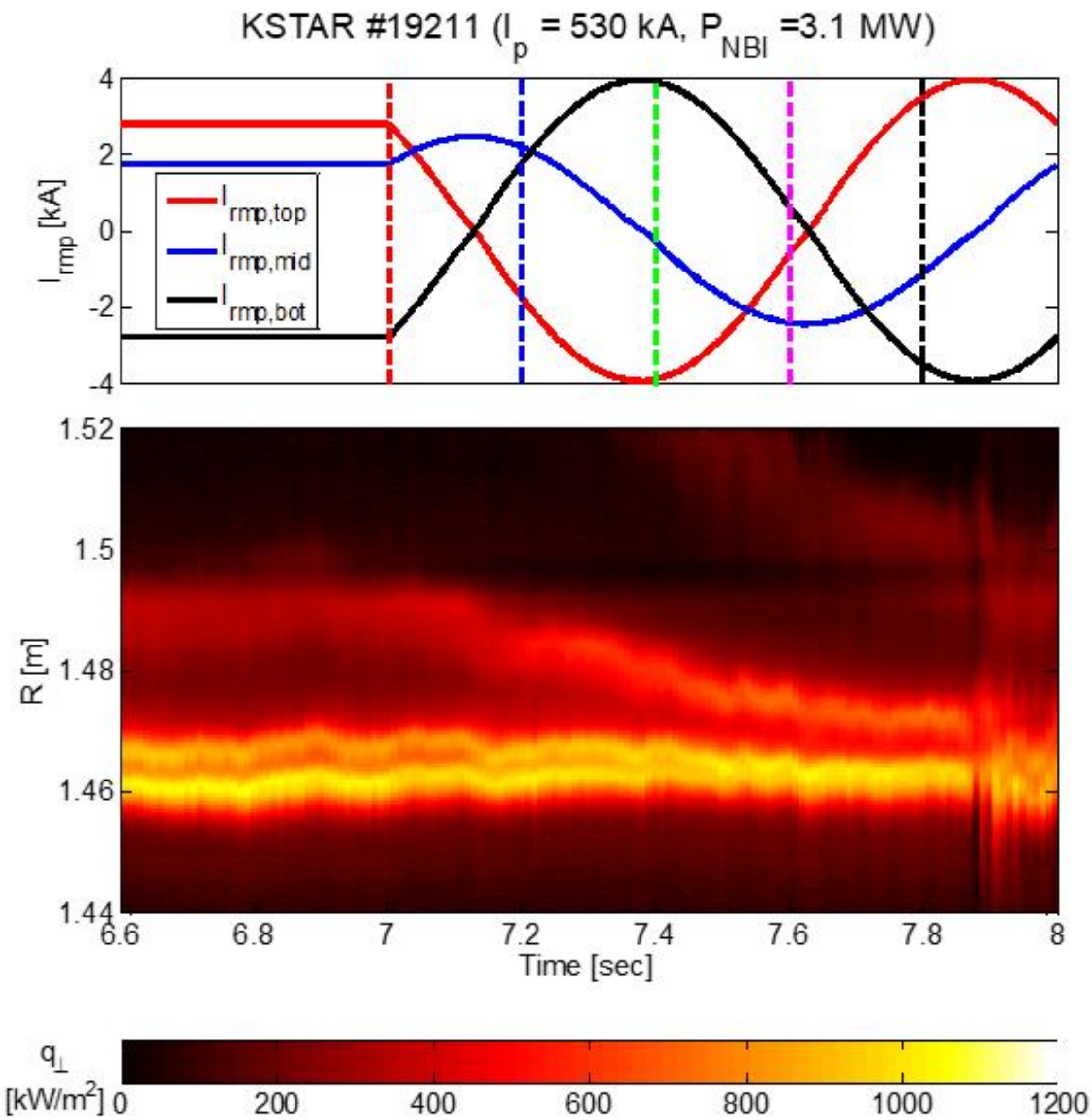

KSTAR #19211 (I_p = 530 kA, P_NBI =3.1 MW)
I_rmp [kA]
I_rmp,top
I_rmp,mid
I_rmp,bot
R [m]
Time [sec]
q_⊥
[kW/m^2]

Fig. 30.

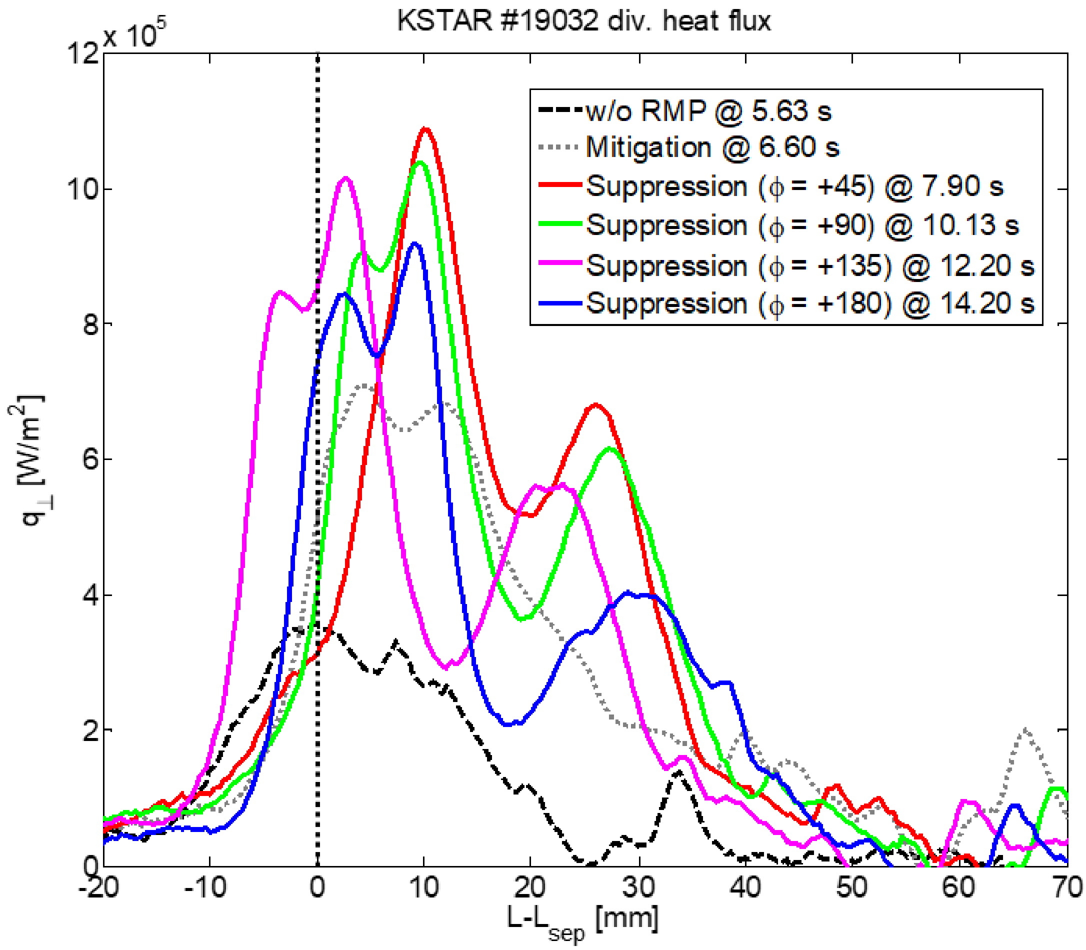

KSTAR #19032 div. heat flux
x 10^5
w/o RMP @ 5.63 s
Mitigation @ 6.60 s
Suppression (ϕ = +45) @ 7.90 s
Suppression (ϕ = +90) @ 10.13 s
Suppression (ϕ = +135) @ 12.20 s
Suppression (ϕ = +180) @ 14.20 s
q⊥ [W/m2]
L-Lsep [mm]

Fig. 31.